Gondwana Research 26 (2014) 505–520

Contents lists available at ScienceDirect

Gondwana Research

journal homepage: www.elsevier.com/locate/gr

Late Cretaceous magmatism in Mamba area, central Lhasa subterrane: Products of back-arc extension of Neo-Tethyan Ocean?☆

Fan-Yi Meng [a,b], Zhidan Zhao [a,b,*], Di-Cheng Zhu [a,b], Xuanxue Mo [a,b], Qi Guan [c], Yu Huang [a,b], Guochen Dong [a,b], Su Zhou [a,b], Donald J. DePaolo [d], T. Mark Harrison [e], Zhaochong Zhang [a,b], Junlai Liu [a,b], Yongsheng Liu [f], Zhaochu Hu [f], Honglin Yuan [g]

[a] State Key Laboratory of Geological Processes and Mineral Resources, China University of Geosciences, Beijing 100083, China
[b] School of Earth Science and Resources, China University of Geosciences, Beijing 100083, China
[c] College of Resources, Shijiazhuang University of Economics, Shijiazhuang 050031, China
[d] Center for Isotope Geochemistry, University of California, Berkeley, CA 94720, USA
[e] Department of Earth and Space Sciences, University of California, Los Angeles, CA 90024, USA
[f] State Key Laboratory of Geological Processes and Mineral Resources, Faculty of Earth Sciences, China University of Geosciences, Wuhan 430074, China
[g] State Key Laboratory of Continental Dynamics, Department of Geology, Northwest University, Xi'an 710069, China

ARTICLE INFO

Article history:
Received 10 March 2013
Received in revised form 8 July 2013
Accepted 14 July 2013
Available online 13 August 2013

Keywords:
Late Cretaceous adakitic rocks and mafic enclaves
Zircon dating
Geochemistry
Mamba
Tibet

ABSTRACT

Cretaceous magmatism in southern Lhasa subterrane, Tibetan plateau has been investigated for many years and a series of models have been proposed to illustrate their petrogenesis and geodynamic implications. But rare work has been done on the Cretaceous magmatism in central Lhasa subterrane. Here we report the petrology, zircon in situ U–Pb geochronology, Hf isotopes, trace element, and whole-rock elements and Sr–Nd isotopic geochemical data of the host granodiorites, and gabbroic and dioritic enclaves in Mamba area, central Lhasa subterrane. Zircon U–Pb dating for a Mamba host granodiorite yields a crystallization age of ~84 Ma, with in situ Hf isotopic analyses for 18 spots of the same zircons of $\varepsilon_{Hf}(t)$ ranging from −7.5 to −0.3. A dioritic enclave (85.2 Ma) is coeval with the host granodiorite and shows similar zircon Hf isotopic compositions ($\varepsilon_{Hf}(t) = -4.0$ to +0.2). Mamba granodiorites (SiO_2 = 66.6–67.5 wt.%) and dioritic enclaves (SiO_2 = 53.9–57.6 wt.%) are high-K calc-alkaline, and a gabbroic enclave is shoshonitic (K_2O = 2.81%). All these samples are metaluminous, and enriched in large ion lithophile elements (LILEs, such as Rb, Ba, K, U, Th) and depleted in high field strength elements (HFSEs, e.g., Nb, Ta, Ti, and Zr). The host granodiorites are enriched in light rare earth elements (REEs), depleted in heavy REEs with weakly negative Eu anomalies (δEu = 0.86–0.88), with high Al_2O_3 (15.0–15.7 wt.%), high Sr/Y ratio (58.1–68.3) and Sr (680–755 ppm), and low Y (10.8–13.0 ppm) abundance, suggesting adakitic affinities. Mamba adakitic granodiorites, gabbroic and dioritic enclaves exhibit homogeneous Sr isotopes ($(^{87}Sr/^{86}Sr)_i$ = 0.7066–0.7067, 0.7073, and 0.7067, respectively) and Nd isotopes ($\varepsilon_{Nd}(t) = -5.7$ to −4.4, −4.0, and −3.6, respectively). These geochemical features allowed us to conclude that the adakitic host granodiorites and mafic (gabbroic–dioritic) enclaves were derived from magma mixing between ancient thickened lower crust and enriched fluid-metasomatized mantle. The distance between Mamba and the suture zone was more than 200 km when the intrusives emplaced at ~85 Ma, which implies that these rocks cannot be resulted from the mid-ocean ridge subduction. Combining of the intra-plate environment indicated by the gabbroic enclave of this study, the presence of the coeval bimodal igneous rocks in the similar latitude in central Lhasa subterrane, and other records in late Cretaceous sedimentary basin, the Mamba ~85 Ma magmatism were attributed to the back-arc extension of Neo-Tethyan Ocean.

1. Introduction

Northward subduction of Neo-Tethyan oceanic lithosphere and related magmatism in Mesozoic, especially during the Late Cretaceous, have been widely discussed in southern Lhasa subterrane in the past two decades (Coulon et al., 1986; Harris et al., 1988, 1990; Quidelleur et al., 1997; Wen et al., 2008a; Ji et al., 2009; Guan et al., 2010; Zhang et al., 2010a; Guan et al., 2011; Zhang et al., 2011; Zhu et al., 2011a; Jiang et al., 2012). The existing interpretations on the petrogenesis

☆ This article belongs to the Special Issue on Orogenesis and metallogenesis in the Sanjiang Tethyan Domain.

* Corresponding author at: School of Earth Science and Resources, China University of Geosciences, 29 Xueyuan Road, Haidian District, Beijing 100083, China. Tel./fax: +86 10 8232 1115.
E-mail address: zdzhao@cugb.edu.cn (Z. Zhao).

1342-937X/$ – see front matter © 2013 International Association for Gondwana Research. Published by Elsevier B.V. All rights reserved.
http://dx.doi.org/10.1016/j.gr.2013.07.017

and tectonomagmatic processes of the Late Cretaceous calc-alkaline granitoids are controversial. They were considered to be generated from partial melting of a newly underplated, mafic lower crust or the subducted Neo-Tethyan basaltic oceanic crust with or without contributions of sediments from different subduction styles of Neo-Tethyan Ocean (low-angle, steep angle, and mid-ocean ridge) (Coulon et al., 1986; Wen et al., 2008a; Zhang et al., 2010a; Zhu et al., 2011a; Jiang et al., 2012). These models are all from the studies of the Late Cretaceous magmatism in southern Lhasa subterrane, however, for that from central Lhasa subterrane, only a few works reported on dating and petrogenesis (Qu et al., 2006; Meng et al., 2010). It is necessary to further constrain the petrogenesis of the Late Cretaceous magmatism in central Lhasa subterrane, to provide a much clear image to the magmatism occurred in both central and southern Lhasa subterranes.

The mafic enclaves which were often occur in calc-alkaline, alkaline and peralkaline granitoids, can provide important information on the nature of the source regions, the mechanism to produce granitic melt, and the evidence of interaction between continental crust and mantle (e.g., Chappell et al., 1987; Holden et al., 1987; Vernon, 1990; Barbarin and Didier, 1992; Yang et al., 2006, 2007; Shellnutt et al., 2010). Currently, magma mixing and/or mingling is prevalently acceptable for the petrogenesis of these mafic enclaves (e.g., Barbarin, 2005; Wang et al., 2012). In the Gangdese batholith in southern Lhasa subterrane, the ~52 Ma Cenozoic "flare-up" magmatism is a typical magma mixing represented by mantle-origin gabbros, micro-granular mafic enclaves (MME) and host granodiorites (Dong et al., 2005; Mo et al., 2005; Dong et al., 2006; Mo et al., 2007).

In this work, we found ~85 Ma coeval mafic enclaves hosted by the granitoids. We present petrology, zircon U–Pb, in situ Hf isotopic, and trace element, and whole-rock element and Sr–Nd isotopic geochemical data of mafic enclaves (gabbroic and dioritic enclaves) and host granodiorites in Mamba area, central Lhasa subterrane. These new data, together with other research in the neighboring regions, allow us to reveal the nature of the magma source, mantle contribution, magma evolution, tectonic setting, as well as the deep geodynamic process occurred during Late Cretaceous in central Lhasa subterrane.

2. Geological background and field observations

The Lhasa Terrane in southern Tibet, which is bounded by Indus–Yarlung Zangbo Suture Zone (IYZSZ) in the south and Bangong–Nujiang Suture Zone (BNSZ) in the north, is the so called southern margin of Asian continent, and have been subducted by Neo-Tethys and further underthrusted by Indian continent (Pan et al., 1983; Girardeau et al., 1985; Pearce and Deng, 1988; Zhao et al., 2009; Zhu et al., 2013). The Lhasa Terrane can be further divided into northern, central, and southern subterranes, separated by the Shiquanhe–Nam Tso Mélange Zone (SNMZ) and Luobadui–Milashan Fault (LMF), respectively (Fig. 1a) (Zhu et al., 2011a, 2013).

The northern Lhasa subterrane is previously inferred to be underlain by a Cambrian or Neoproterozoic crystalline (Amdo orthogneiss) basement in the Amdo area (Xu et al., 1985; Dewey et al., 1988; Guynn et al., 2006, 2012), but recently identified that the Amdo microcontinent is no longer a part of the Lhasa Terrane (Zhu et al., 2013). This subterrane is characterized by the existence of juvenile crust (Zhu et al., 2011a) and is covered by Middle Triassic to Cretaceous sedimentary rocks with abundant Early Cretaceous volcanic rocks and associated intrusives (Pan et al., 2004; Zhu et al., 2013).

The central Lhasa subterrane was once a microcontinent with Proterozoic and Archean basement rocks (Zhu et al., 2009a, 2011a, 2013). These basement rocks (e.g., part of the Nyainqêntanglha Group) have experienced multiphase metamorphism during the Neoproterozoic (~720 Ma; Zhang et al., 2010b; ~690 Ma, Dong et al., 2011a; ~650 Ma, Zhang et al., 2012, 2013), Late Triassic (225–213 Ma; Dong et al., 2011b), and Cenozoic (Xu et al., 1985; Kapp et al., 2005). This reworked crystalline basement is covered with widespread Permo-Carboniferous metasedimentary rocks and Upper Jurassic-Lower Cretaceous sedimentary rocks with abundant volcanic rocks and associated granitoids (Zhu et al., 2009a, 2011a, 2013), plus minor but well-exposed Ordovician, Silurian, Devonian, and Triassic limestone (Pan et al., 2004).

The southern Lhasa subterrane is characterized by the existence of juvenile crust (Mo et al., 2008; Zhu et al., 2011a) and by the absence of Precambrian crystalline basement (cf. Zhu et al., 2013), which is dominated by the Cretaceous-Tertiary Gangdese Batholith and Paleocene Linzizong volcanic succession (Mo et al., 2007, 2008; Zhu et al., 2011a, and references therein) with minor Triassic-Cretaceous volcano-sedimentary rocks that are largely restricted to its eastern part (Pan et al., 2004; Zhu et al., 2013).

The Lhasa Terrane is widely considered not only as an archetype of a Cenozoic orogen resulting from the India–Asia continental collision marked by the IYZSZ, but also a pre-Cretaceous Andean-type active continental margin genetically associated with the northward subduction of the Neo-Tethyan lithosphere (Allègre et al., 1984; Sengör, 1987; Yin and Harrison, 2000; Chung et al., 2005). Recent studies indicate that the northward Neo-Tethyan subduction is likely initialized in the very Early Cretaceous triggered by the Lhasa–Qiangtang collision and that much of the Mesozoic magmatism in the Lhasa Terrane can be attributed to the southward subduction of the Bangong–Nujiang Tethyan lithosphere beneath the Lhasa Terrane, which likely began in the late Middle Permian triggered by the Lhasa–Australia collision and ceased in the late Early Cretaceous (Zhu et al., 2009a,b, 2011b, 2013). Tectonically, both the northern and southern Lhasa subterranes experienced significant crustal shortening (>50% and >40%, respectively) during a period from the Late Cretaceous to Paleocene (Kapp et al., 2003; He et al., 2007; Volkmer et al., 2007).

Samples investigated in this study were collected in Mamba area (Fig. 1a), eastern central Lhasa subterrane, where was mainly composed of Pre-Ordovician strata, Carboniferous metasedimentary rocks, Upper Permian Luobadui formation, Upper Cretaceous Shexing formation (also named Takena formation) and Middle Eocene Pana formation. The magmatism in Mamba area includes Late Triassic granitoids, Late Jurassic granitoids and Late Cretaceous granitoids. The Late Cretaceous igneous rocks in Mamba intruded in Pre-Ordovician schist and Late Triassic monzonitic granites. The samples collected in this study (N30°04′23.2″–N30°02′01.8″, E92°09′14.7″–E92°05′49.0″) close to the previously reported samples (MB12; N30°04′30.9″, E92°09′14.9″; Fig. 1b, Meng et al., 2010). The Mamba intrusives consist of gabbroic and dioritic enclaves, and host granodiorites. The granodiorites are gray to white, medium-grain (Fig. 2a), undeformed, which typically contain quartz (~30% in volume), plagioclase (25–30%), alkali-feldspar (10–15%), biotite (5–10%), amphibole (5–10%), and accessory minerals (zircon and titanite, <1%) (Fig. 2b). Gabbroic and dioritic enclaves are round or elliptoid in shape and sharply contacting with the host rocks (Fig. 2a), in the size of up to 8 cm in diameter. These enclaves contain plagioclase, amphibole and biotite (Fig. 2c and d), showing igneous textures (needle-like apatite and local quartz, with K-feldspar megacrysts up to 4 cm × 6 cm; Fig. 2a), which are identical to the textures of magma mixing processes described from other mafic enclaves around the world (Vernon, 1984; Mo et al., 2005, 2007; Yang et al., 2007; Kocak et al., 2011). Despite the pyroxene that is absent in our gabbroic enclave, the gabbroic enclave has the similar composition with gabbros, so in this paper we call it "gabbroic enclave".

3. Analytical methods

3.1. LA–ICP-MS zircon U–Pb dating

One granodiorite sample and one dioritic enclave sample were selected for zircon U–Pb and Hf isotope analysis. Zircons were separated by heavy-liquid and magnetic methods. Cathodoluminescence (CL) images were taken at the Institute of Geology, Chinese Academy of Geological Sciences (Beijing) for checking internal structures of individual

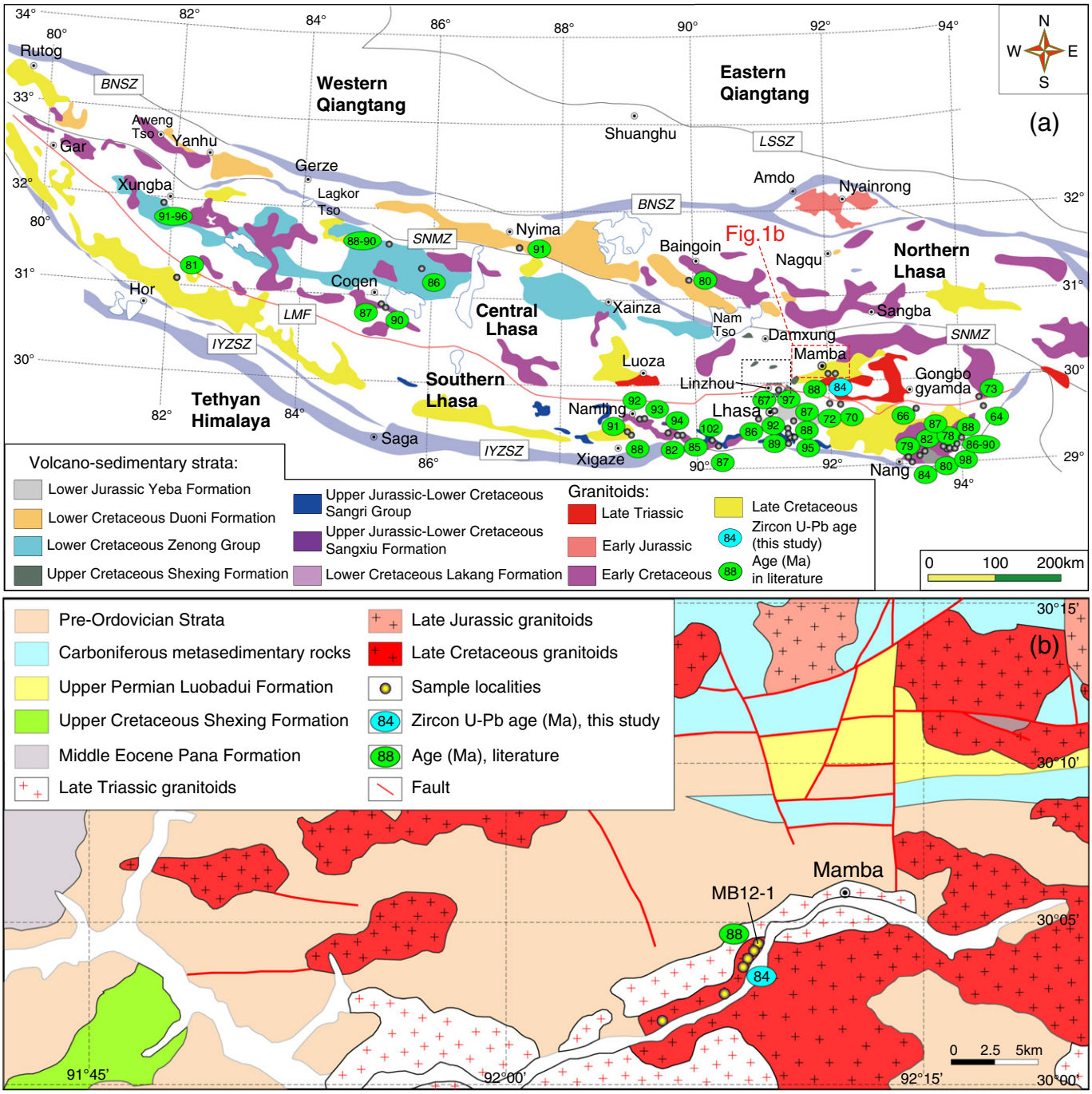

Fig. 1. (a) Tectonic framework of the Tibetan Plateau (modified from Zhu et al., 2013) showing the major tectonic subdivisions, distribution of suture zones, and localities of dated late cretaceous igneous rocks (ovals with numerals). LSSZ = Longmu Tso–Shuanghu Suture Zone; BNSZ = Bangong–Nujiang Suture Zone; SNMZ = Shiquan River–Nam Tso Mélange Zone; LMF = Luobadui–Milashan Fault; IYZSZ = Indus–Yarlung Zangbo Suture Zone. Literature data are from: Qu et al. (2006), Wen et al. (2008b), Ji et al. (2009), Lee et al. (2009), Guan et al. (2010), Huang et al. (2010), Ma and Yue (2010), Meng et al. (2010), Zhang et al. (2010a), Gao et al. (2011), Guan et al. (2011), Liu et al. (2011), Yu et al. (2011), Zhu et al. (2011a), and Jiang et al. (2012). (b) Geological map of Mamba area (modified from Yang et al., 2005).

zircons and for selecting the appropriate spots for zircon isotope analyses.

Zircon U–Pb dating was performed by LA–ICP-MS at the State Key Laboratory of Geological Processes and Mineral Resources, China University of Geosciences, Wuhan (GPMR Wuhan). Detailed operating conditions for the laser ablation system and the ICP-MS instrument and data reduction are the same as description by Liu et al. (2008, 2010). Laser sampling was performed using a GeoLas 2005. An Agilent 7500a ICP-MS instrument was used to acquire ion-signal intensities. Helium was applied as a carrier gas. Argon was used as the make-up gas and mixed with the carrier gas via a T-connector before entering the ICP. Nitrogen was added into the central gas flow (Ar + He) of the Ar plasma to decrease the detection limit and improve precision (Hu et al., 2008). Each analysis incorporated a background acquisition of approximately 20–30 s (gas blank) followed by 50 s data acquisition from the sample. The Agilent Chemstation was utilized for the acquisition of each individual analysis. Off-line selection and integration of background and analyze signals, and time-drift correction and U–Pb dating were performed by *ICPMSDataCal* (Liu et al., 2008, 2010).

Zircon 91500 was used as external standard for U–Pb dating, and was analyzed twice every 6 analyses. Time-dependent drifts of U–Th–Pb isotopic ratios were corrected using a linear interpolation (with

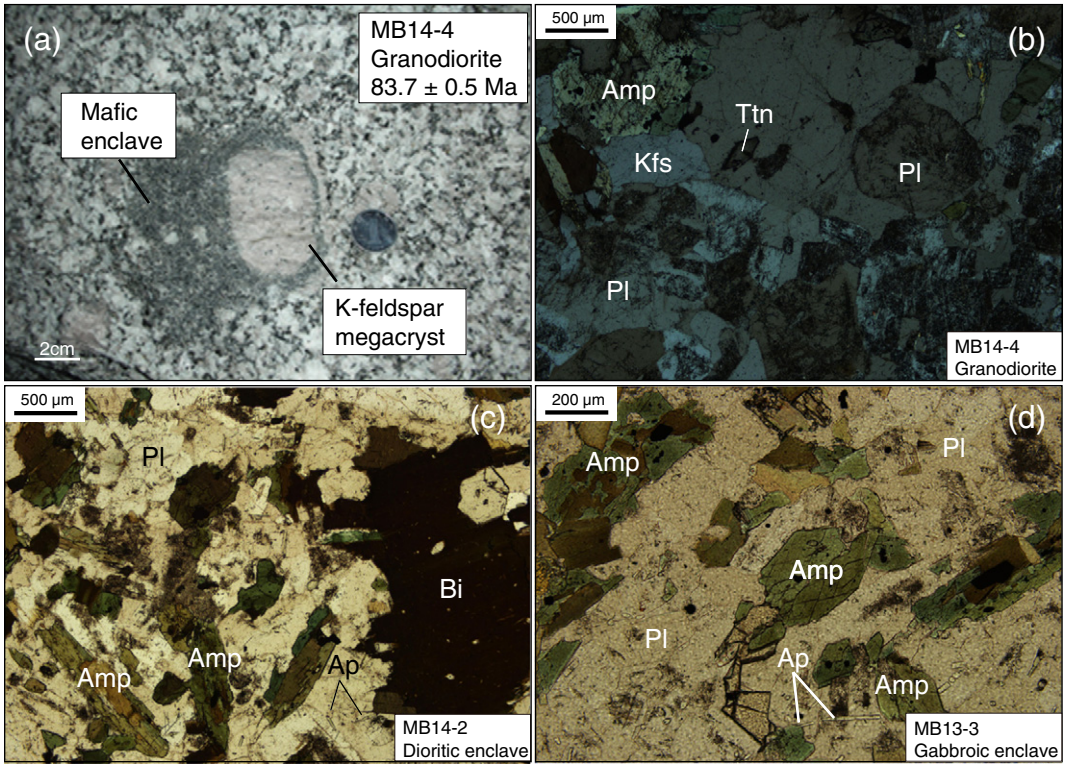

Fig. 2. (a) Field observations of Mamba host granodiorite and dioritic enclave; (b–d) photomicrographs of Mamba granodiorite, dioritic and gabbroic enclaves. Abbreviations: Amp = amphibole; Kfs = K-feldspar; Pl = plagioclase; Bi = biotite; Ap = apatite; Ttn = titanite.

time) for every six analyses according to the variations of 91500 (i.e., 2 zircon 91500 + 6 samples + 2 zircon 91500) (Liu et al., 2010). Preferred U–Th–Pb isotopic ratios used for 91500 are from Wiedenbeck et al. (1995). Uncertainty of preferred values for the external standard 91500 was propagated to the ultimate results of the samples. Common lead was corrected for using the correction function (Andersen, 2002). ISOPLOT (version 3.0) (Ludwig, 2003) was used for plotting concordia diagrams and age spectra, and for age calculations. Uncertainties on individual analyses are reported as 1-sigma; mean ages for pooled $^{206}Pb/^{238}U$ results are reported as 2 sigma's. The zircon U–Pb isotopic data and trace-element are summarized in Tables 1 and 2.

3.2. Whole-rock geochemical analysis

Whole rock samples were first crushed to less than 5 mm in a corundum jaw crusher. About 100 g was powdered in a vibratory disk mill equipped with a tungsten carbide milling cup to less than 200 mesh. Major elements were analyzed by X-ray fluorescence (Rikagu RIX 2100) at the State Key Laboratory of Continental Dynamics, Northwest University, China (CDNU). Analytic precision and accuracy for major elements are the same as Rudnick et al. (2004).

Trace element analyses were conducted by LA–ICP-MS at GPMR Wuhan. About 60 g was powdered in an agate ring mill to less than 200 mesh. The samples were then digested by HF + HNO_3 in Teflon bombs and analyzed with an Agilent 7500a ICP-MS. Element contents were calibrated against multiple-reference materials (BCR-2G, BIR-1G, and BHVO-2G) without applying internal standardization (Liu et al., 2008). Detailed operating conditions for the laser ablation system and the ICP-MS instrument and data reduction are the same as in the description by Liu et al. (2008).

Whole-rock Sr–Nd isotopic compositions were determined using a Finnigan MAT-261 mass spectrometer operated in static mode at GPMR Wuhan. Analytical details were given in Rudnick et al. (2004) and Liu et al. (2004). Sr and Nd isotopic fractionation was normalized to $^{86}Sr/^{88}Sr = 0.1194$ and $^{146}Nd/^{144}Nd = 0.7219$, respectively. The average $^{143}Nd/^{144}Nd$ ratio of the La Jolla standard measured during the sample runs is 0.511862 ± 5 (2-sigma), and the average $^{87}Sr/^{86}Sr$ ratio of the NBS-987 standard is 0.710236 ± 16 (2-sigma). Total procedural Sr and Nd blanks are <1 ng and <50 pg, respectively. The whole-rock compositional data are listed in Table 3.

3.3. Zircon Hf isotopic analysis

Hf isotope measurements were done on the same spots or the same age domains for age determinations of the concordant grains, as guided by CL images. Zircons were analyzed using a Nu Plasma HR MC–ICP-MS (Nu Instruments Ltd., UK), coupled to a GeoLas 2005 excimer ArF laser-ablation system with a beam size of 44 μm and the laser pulse frequency of 8 Hz at CDNU. During the analysis, the measured values of well-characterized zircon standards (91500, GJ-1, and Monastery) agree with the recommended values to within $2\sigma_n$. The obtained Hf isotopic compositions were 0.282016 ± 20 ($2\sigma_n$, n = 84) for the GJ-1 standard and 0.282735 ± 24 ($2\sigma_n$, n = 84) for the Monastery standard, respectively, agreeing with the recommended values to within $2\sigma_n$ (cf. Yuan et al., 2008). Initial $^{176}Hf/^{177}Hf$ ratios and $\varepsilon_{Hf}(t)$ values were calculated with the reference to the chondritic reservoir (CHUR) at the time of zircon growth from magmas. The decay constant for ^{176}Lu of 1.867×10^{-11} year^{-1} (Söderlund et al., 2004), the chondritic $^{176}Hf/^{177}Hf$ ratio of 0.282785 and $^{176}Lu/^{177}Hf$ ratio of 0.0336 (Bouvier et al., 2008) were adopted. Depleted mantle model ages (T_{DM}) used for basic to intermediate rocks were calculated with reference to the depleted mantle at a present-day $^{176}Hf/^{177}Hf$ ratio of 0.28325, similar to that of the average MORB (Nowell et al., 1998) and $^{176}Lu/^{177}Hf = 0.0384$ (Griffin et al., 2000). For each zircon, we also calculated the Hf isotope "crustal" model age (T^{C}_{DM}), by assuming its parental magma to have been derived from an average continental crust, with $^{176}Lu/^{177}Hf = 0.015$, that originated from the depleted mantle source (Griffin et al., 2002). Our conclusions will not be affected even if other decay constants were used. The zircon Lu–Hf isotopic data are given in Table 4.

Table 1
Zircon LA–ICP-MS U–Pb data of the Late Cretaceous Mamba magmatic rocks.

Spot	Pb	Th	U	Th/U	$^{207}Pb^{a}/^{206}Pb^{a}$		$^{207}Pb^{a}/^{235}U^{a}$		$^{206}Pb^{a}/^{238}U^{a}$		$^{207}Pb^{a}/^{206}Pb^{a}$		$^{207}Pb^{a}/^{235}U^{a}$		$^{206}Pb^{a}/^{238}U^{a}$	
	ppm	ppm	ppm		Ratio	±1σ	Ratio	±1σ	Ratio	±1σ	Age	±1σ	Age	±1σ	Age	±1σ
MB14-4, host granite, 18 spots, mean = 83.7 ± 0.5 Ma, MSWD = 0.3																
1	9.90	602	610	0.99	0.0483	0.0017	0.0865	0.0031	0.0130	0.0001	113	63	84	3.0	83.2	0.9
2	10.9	692	656	1.05	0.0473	0.0026	0.0860	0.0049	0.0131	0.0002	64	99	84	5.0	84.0	1.0
3	11.7	762	705	1.08	0.0491	0.0017	0.0881	0.0030	0.0130	0.0001	154	61	86	3.0	83.5	0.9
4	8.67	504	535	0.94	0.0508	0.0018	0.0905	0.0031	0.0130	0.0001	231	59	88	3.0	83.2	0.9
5	5.62	246	352	0.70	0.0480	0.0034	0.0866	0.0064	0.0130	0.0002	101	132	84	6.0	83.0	1.0
6	8.86	504	526	0.96	0.0469	0.0023	0.0850	0.0044	0.0131	0.0003	43	78	83	4.0	84.0	2.0
7	7.47	351	491	0.71	0.0481	0.0020	0.0854	0.0037	0.0131	0.0004	102	54	83	3.0	84.0	2.0
8	6.23	277	416	0.67	0.0490	0.0023	0.0868	0.0040	0.0129	0.0002	150	83	84	4.0	82.6	1.0
9	8.05	453	504	0.90	0.0477	0.0016	0.0856	0.0028	0.0131	0.0001	86	59	83	3.0	83.8	0.8
10	10.8	647	667	0.97	0.0471	0.0015	0.0855	0.0027	0.0132	0.0001	52	52	83	3.0	84.8	0.8
11	8.75	438	566	0.77	0.0462	0.0017	0.0826	0.0030	0.0131	0.0001	8	55	81	3.0	83.7	0.8
12	8.76	476	547	0.87	0.0490	0.0017	0.0882	0.0029	0.0132	0.0002	148	55	86	3.0	84.3	1.0
13	7.99	446	501	0.89	0.0504	0.0016	0.0904	0.0028	0.0131	0.0001	214	54	88	3.0	83.6	0.8
14	9.38	456	619	0.74	0.0451	0.0015	0.0814	0.0027	0.0132	0.0002	−13	46	79	3.0	84.3	1.0
15	13.2	852	798	1.07	0.0473	0.0020	0.0851	0.0036	0.0130	0.0002	63	64	83	3.0	83.0	1.0
16	7.80	360	504	0.71	0.0465	0.0024	0.0847	0.0044	0.0132	0.0002	23	81	83	4.0	84.0	1.0
17	7.61	341	501	0.68	0.0479	0.0022	0.0856	0.0037	0.0131	0.0002	96	74	83	3.0	84.0	1.0
18	9.99	522	627	0.83	0.0487	0.0020	0.0873	0.0034	0.0131	0.0002	133	63	85	3.0	84.0	1.0
MB14-2, dioritic enclave, 17 spots (without spot 11), mean = 85.2 ± 0.4 Ma, MSWD = 1.2																
1	5.35	243	336	0.72	0.0490	0.0041	0.0901	0.0077	0.0133	0.0002	149	165	88	7.0	85.0	1.0
2	6.97	383	436	0.88	0.0497	0.0026	0.0894	0.0047	0.0131	0.0002	179	98	87	4.0	83.8	1.0
3	4.88	210	325	0.65	0.0488	0.0021	0.0876	0.0037	0.0134	0.0003	136	58	85	3.0	86.0	2.0
4	48.9	4294	2422	1.77	0.0471	0.0023	0.0865	0.0041	0.0133	0.0001	52	106	84	4.0	85.4	0.8
5	62.8	6271	2912	2.15	0.0487	0.0010	0.0903	0.0019	0.0134	0.0001	134	34	88	2.0	85.9	0.6
6	6.00	262	396	0.66	0.0505	0.0041	0.0911	0.0072	0.0131	0.0002	218	184	89	7.0	84.0	1.0
7	6.51	278	430	0.65	0.0471	0.0019	0.0875	0.0034	0.0135	0.0002	54	62	85	3.0	87.0	1.0
8	7.89	417	498	0.84	0.0477	0.0017	0.0881	0.0032	0.0134	0.0001	83	64	86	3.0	85.9	0.8
9	9.27	555	545	1.02	0.0558	0.0026	0.1031	0.0045	0.0135	0.0002	442	72	100	4.0	86.0	1.0
10	12.1	513	616	0.83	0.0480	0.0016	0.0872	0.0026	0.0133	0.0001	98	54	85	2.0	85.2	0.8
11	60.3	242	623	0.39	0.0667	0.0012	0.8199	0.0150	0.0891	0.0010	827	21	608	8.0	550	6.0
12	9.78	579	605	0.96	0.0506	0.0016	0.0920	0.0029	0.0132	0.0001	224	54	89	3.0	84.5	0.8
13	8.52	434	533	0.81	0.0480	0.0026	0.0881	0.0049	0.0132	0.0002	99	101	86	5.0	85.0	1.0
14	8.92	507	548	0.92	0.0499	0.0041	0.0900	0.0070	0.0132	0.0002	191	148	87	6.0	84.0	1.0
15	12.0	730	698	1.05	0.0460	0.0019	0.0841	0.0036	0.0133	0.0002	−3	57	82	3.0	85.0	1.0
16	11.8	692	712	0.97	0.0471	0.0018	0.0871	0.0035	0.0133	0.0001	55	71	85	3.0	85.4	0.8
17	7.74	388	492	0.79	0.0466	0.0025	0.0834	0.0043	0.0130	0.0001	30	114	81	4.0	83.1	0.8
18	15.0	770	950	0.81	0.0468	0.0020	0.0863	0.0036	0.0134	0.0001	37	74	84	3.0	85.8	0.7

[a] Radiogenic lead, isotopic ratios and ages were corrected by common lead, following the methods reported by Andersen (2002).

4. Results

4.1. Zircon U–Pb dating

The zircon grains from a host granodiorite (MB14-4) are mostly euhedral and show short prismatic forms (100–200 μm long) with an aspect ratio of 2:1 to 3:1 (Fig. 3a). While the zircons in dioritic enclave (MB14-2) are apparently smaller than that in the host granodiorite and exhibited subidiomorphic or xenomorphic (80–200 μm long), with an aspect ratio of 2:1 to 3:1. Some of them displayed inherited core (Fig. 3b). All the zircon grains exhibit clear oscillatory zoning (Fig. 3).

The analyzed zircons from both host rock and dioritic enclave had varying uranium (325–2912 ppm) and thorium (210–6271 ppm) contents, with Th/U ratios ranging from 0.39 to 2.15 (Table 1), which is consistent with a magmatic origin (Hoskin and Schaltegger, 2003). Eighteen analyses from the host rock (MB14-4) yield concordant $^{206}Pb/^{238}U$ ages ranging from 82.6 to 84.8 Ma (Fig. 3c), with a weighted mean of 83.7 ± 0.5 Ma (MSWD = 0.3). Zircon grains from dioritic enclave (MB14-2) yielded concordant $^{206}Pb/^{238}U$ ages of 83.1–87.0 Ma (17 spots) with a weighted mean of 85.2 ± 0.4 Ma (MSWD = 1.2) (Fig. 3d), excluding one spot with inherited age (550 Ma). We interpret these two ages as emplacement ages of the host granodiorite and dioritic enclave, respectively.

Zircon grains from host granodiorite and dioritic enclave showed fractionated REE patterns of heavy REE enrichment and light REE depletion, with clear positive Ce and insignificant negative Eu anomalies (Fig. 3e and f; Table 2), as observed in magmatic zircons (Hoskin and Schaltegger, 2003).

4.2. Whole-rock geochemistry

The Mamba samples are granodiorite, syenite–diorite, and gabbro, by the plot of total alkalis against silicon contents (TAS, Fig. 4a). The granodiorite shows homogeneous major element compositions (SiO_2 = 66.6–67.5 wt.%, Al_2O_3 = 15.0–15.7 wt.%, MgO = 1.68–1.89 wt.%, and $Mg^{\#}$ = 48). They have high K_2O (2.57–3.63 wt.%), K_2O/Na_2O (0.62–0.9), and A/CNK values (0.90–0.92; Fig. 4b), suggesting that they are high-K calc-alkaline metaluminous granodiorites (Fig. 5a). The gabbroic enclave is shoshonitic, with low SiO_2 (51.5 wt.%), high MgO (5.25 wt.%), K_2O (2.81 wt.%), and TiO_2 (1.34 wt.%) (Fig. 5a). The dioritic enclaves belong to high-K calc-alkaline to shoshonitic series, having moderate SiO_2 (53.9–57.6 wt.%), high K_2O (1.83–3.61 wt.%) and Na_2O (Na_2O = 3.94–4.75 wt.%). All the mafic enclaves are metaluminous rocks (A/CNK = 0.74–0.84; Fig. 4b).

The host granodiorite displays low heavy REEs (Yb = 0.95–1.23 ppm; Y = 10.8–13.0 ppm) and high Sr abundance (680–755 ppm) and Sr/Y ratios (58–68), indicating that they can be classified as adakitic rocks defined by Defant and Drummond (1990) (Fig. 6). The granodiorite samples exhibit low abundances of compatible trace elements (Cr = 26.5–31.1 ppm; Ni = 12.0–14.1 ppm). The gabbroic enclave is characterized by high Zr abundance (263 ppm) and Zr/Y ratio (~9) (Fig. 7). In the chondrite-normalized REE (Fig. 8a) and the primitive mantle-normalized trace element diagram (Fig. 8b), all the

Table 2
Zircon trace element data of the Late Cretaceous Mamba magmatic rocks.

Spot	La	Ce	Pr	Nd	Sm	Eu	Gd	Tb	Dy	Ho	Er	Tm	Yb	Lu
MB14-4 01	0.01	32.37	0.03	0.74	1.41	0.77	8.72	2.74	35.12	13.44	76.72	17.78	200.15	45.32
MB14-4 02	0.00	33.94	0.07	0.76	1.53	0.78	9.11	2.98	36.36	14.56	80.46	18.25	206.73	47.09
MB14-4 03	0.15	45.24	0.08	1.39	2.58	1.08	14.20	4.62	59.48	22.56	125.53	28.53	312.65	66.54
MB14-4 04	21.07	65.91	3.75	15.19	4.91	1.46	16.11	4.80	58.80	23.12	126.95	29.75	331.25	73.14
MB14-4 05	0.12	21.17	0.05	0.72	0.99	0.45	6.13	1.85	27.33	11.68	69.32	17.60	210.75	47.11
MB14-4 06	3.22	38.18	0.63	3.55	2.18	0.70	7.97	2.64	32.06	12.38	70.22	16.36	181.35	38.43
MB14-4 07	0.02	24.01	0.02	0.60	1.42	0.54	8.36	2.74	37.33	15.35	90.21	22.62	266.62	59.69
MB14-4 08	0.02	20.19	0.02	0.42	1.11	0.57	6.58	2.05	29.60	12.64	75.71	18.67	225.18	52.98
MB14-4 09	0.04	26.57	0.09	1.63	2.91	1.06	13.21	4.03	50.98	19.84	111.10	26.81	302.88	66.32
MB14-4 10	0.01	31.69	0.05	0.73	1.62	0.58	8.82	2.86	36.93	14.69	82.33	20.15	228.71	50.86
MB14-4 11	0.01	30.66	0.04	0.68	1.24	0.74	8.86	3.06	42.07	18.12	107.65	27.20	317.31	71.06
MB14-4 12	0.05	34.38	0.06	1.08	1.84	0.81	10.35	3.50	46.63	19.04	107.63	26.09	298.10	65.67
MB14-4 13	0.70	29.88	0.15	1.42	1.88	0.86	11.00	3.55	47.40	19.12	108.86	26.42	303.02	65.44
MB14-4 14	0.01	33.43	0.04	0.67	1.53	0.65	8.13	2.94	40.56	17.65	106.28	27.17	325.18	70.30
MB14-4 15	0.13	40.58	0.08	1.53	2.01	0.95	10.83	3.32	41.23	16.18	88.51	21.26	241.64	50.11
MB14-4 16	0.00	25.92	0.05	0.79	1.53	0.72	9.06	3.02	40.27	16.79	96.98	25.22	294.39	61.34
MB14-4 17	0.01	29.92	0.04	0.57	1.81	0.71	9.86	3.27	46.43	19.16	111.33	28.30	336.70	69.15
MB14-4 18	0.01	37.91	0.03	0.93	1.58	0.84	10.43	3.49	46.95	18.89	106.30	26.49	305.41	61.38
MB14-2 01	0.03	20.85	0.02	0.43	1.09	0.36	4.70	1.86	25.78	10.50	62.12	15.48	182.20	43.43
MB14-2 02	0.03	24.78	0.02	0.37	1.00	0.55	5.93	1.92	26.54	10.55	58.91	13.91	153.48	36.68
MB14-2 03	0.01	18.55	0.02	0.32	0.98	0.46	5.98	2.16	30.24	12.74	76.83	19.36	218.57	51.96
MB14-2 04	1.39	104.93	0.80	6.62	8.00	3.86	32.73	9.52	112.49	39.77	200.71	41.72	410.47	83.63
MB14-2 05	0.13	104.08	0.25	4.12	7.59	3.78	34.00	9.60	111.07	38.25	190.48	39.87	397.59	77.74
MB14-2 06	21.12	55.76	3.58	14.44	3.07	0.84	8.19	2.42	32.71	13.20	75.86	18.52	212.75	45.76
MB14-2 07	0.02	21.35	0.03	0.63	1.56	0.63	7.77	2.77	36.04	15.10	90.81	22.62	265.17	61.67
MB14-2 08	0.79	28.28	0.14	1.18	1.18	0.53	6.31	2.08	26.79	10.99	62.72	14.72	168.63	40.31
MB14-2 09	31.30	63.60	2.48	9.82	5.05	2.18	19.34	5.90	71.93	27.78	153.75	34.01	378.84	84.27
MB14-2 10	0.01	35.18	0.05	0.69	1.66	0.68	9.16	3.11	41.21	17.32	101.31	24.63	283.30	66.03
MB14-2 11	0.44	10.40	0.20	2.53	4.69	0.74	27.12	8.72	113.04	42.58	219.42	43.50	410.94	81.23
MB14-2 12	2.50	45.16	0.72	3.73	2.53	0.98	12.86	4.36	58.80	24.13	137.39	31.75	348.41	77.29
MB14-2 13	1.08	27.40	0.26	1.30	1.41	0.63	6.10	2.19	27.19	10.83	61.83	15.11	172.13	39.88
MB14-2 14	0.43	30.46	0.18	3.66	6.21	2.22	25.39	7.91	97.40	36.98	188.47	42.13	435.82	84.83
MB14-2 15	0.00	38.59	0.08	1.01	2.07	0.76	10.13	3.07	37.62	14.54	80.34	19.15	214.05	46.38
MB14-2 16	0.03	32.41	0.02	0.78	1.24	0.56	7.41	2.37	30.18	12.07	67.03	15.95	184.18	41.88
MB14-2 17	0.10	26.22	0.11	1.83	3.45	1.38	16.49	5.29	67.69	25.81	141.02	32.76	354.46	71.25
MB14-2 18	0.03	45.35	0.06	0.93	2.15	0.90	12.24	4.12	52.54	20.71	113.75	26.38	297.25	63.28

samples show similar patterns, with enriched light REE and LILEs, without apparent negative Eu anomalies ($\delta Eu = 0.82–0.96$) as well as depleted in HFSEs, such as Nb, Ta, and Ti. It is important to note that the REE abundances of the mafic enclaves are higher than that of the host granodiorites (234–370 ppm, 186–216 ppm, respectively; Fig. 8a).

Initial $^{87}Sr/^{86}Sr$ and $\varepsilon_{Nd}(t)$ values are calculated to 85 Ma. The host granodiorites have initial $^{87}Sr/^{86}Sr$ values of 0.706620 to 0.706729 and $\varepsilon_{Nd}(t)$ values of −5.7 to −4.4 (Table 3), while the gabbroic and dioritic enclaves have similar Sr–Nd isotopic compositions ($(^{87}Sr/^{86}Sr)_i$ = 0.706668 to 0.707260, $\varepsilon_{Nd}(t) = -4.0$ to −3.6, Table 3).

4.3. Zircon Hf isotopes

Eighteen spots on zircons from the host granodiorite (MB14-4) show negative $\varepsilon_{Hf}(t)$ values (−7.5 to −0.3), corresponding to the mesoproterozoic Hf crustal model ages (T^C_{DM} = 1.1–1.6 Ga, Table 4); the dioritic enclave displays identical zircon Hf isotopes ($\varepsilon_{Hf}(t) = -4.0$ to +0.2, Table 4). The zircon Hf isotopic compositions of the Mamba igneous rocks from the central Lhasa subterrane were distinctly different from those of the coeval igneous from Milin and Kelu in southern Lhasa subterrane (78–84 Ma and 92 Ma; $\varepsilon_{Hf}(t) = +0.2$ to +15.1 and +9.3 to +15.8; Guan et al., 2010; Zhu et al., 2011a; Jiang et al., 2012) and Nyima in northern Lhasa subterrane (91 Ma; $\varepsilon_{Hf}(t) = +5.2$ to +8.2; Wang and Zhu, unpublished data).

5. Discussion

5.1. Late Cretaceous magmatism in the Lhasa Terrane

Late Cretaceous magmatism in central Lhasa subterrane has been reported in Mamba by Meng et al. (2010) and in Coqen (Qu et al., 2006; Lee et al., 2009). Meanwhile, some ultrapotassic rocks in Xungba, west of the central Lhasa subterrane, contain abundant inherited zircons with Late Cretaceous age (Liu et al., 2011). In northern Lhasa subterrane, the Late Cretaceous magmatism has only been found near Nyima (Ma and Yue, 2010; Yu et al., 2011; Wang and Zhu, unpublished data) and Baingoin (Gao et al., 2011). On the contrary, abundant Late Cretaceous magmatic rocks have been found in southern Lhasa subterrane recently (Fig. 1; e.g., Coulon et al., 1986; Harris et al., 1988, 1990; Quidelleur et al., 1997; Wen et al., 2008a; Ji et al., 2009; Lee et al., 2009; Guan et al., 2010; Huang et al., 2010; Zhang et al., 2010a; Guan et al., 2011; Zhu et al., 2011a; Jiang et al., 2012). In addition, newly identified coeval bimodal igneous rocks (diabase and leucogranite dikes) were found in Namling, in the north of the southern Lhasa subterrane (Ye, 2013). The Late Cretaceous magmatism outcrops have been illustrated in Fig. 1a, from which, age-spatial distribution reveals the presence of W–E trend of belt of large-scale Late Cretaceous magmatism in central and southern Lhasa subterranes.

5.2. Petrogenesis

5.2.1. Mafic enclaves and magma mixing

The dioritic and gabbroic enclaves occurring in Mamba have similar major and trace elements as well as isotopic component except that the gabbroic enclave has the lowest SiO_2 content and the highest Zr abundance. So here we called both dioritic and gabbroic enclaves together as “mafic enclaves”.

There are many interpretations relating to the origin of mafic enclaves, including xenoliths of the country rocks (e.g., Bacon, 1986; Xu et al., 2006), refractory and residual phase assemblages derived from granitoid sources (e.g., Chappell et al., 1987), cumulates formed by early crystallization (e.g., Bonin, 1991; Schonenberger et al., 2006), and

generated during magma mixing between mafic and felsic magmas (e.g., Holden et al., 1987; Wiebe et al., 1997; Barbarin, 2005; Yang et al., 2006, 2007; Kent et al., 2010; Kocak et al., 2011; Wang et al., 2012).

The Mamba mafic enclaves (~85 Ma) were coeval with the host granodiorites (~84 Ma), precluding the possibility of xenoliths coming from country rocks. Petrological observations illustrate that the mafic enclaves have igneous textures, with K-feldspar megacrysts in the enclaves (Fig. 2a) and needle-like apatite in the matrix (Fig. 2c and d), demonstrating that externally injected magmatic globules into the felsic host magma while they are both in "soft state" before crystallization (Vernon, 1984; Elburg, 1996; Perugini et al., 2003). Meanwhile, the experiments (Wyllie et al., 1962) suggest that long prismatic-acicular apatites result from strong undercooling during growth, and this is commonly taken as indirect evidence of magma-mixing reflecting quenching of the basic melt by cooler acidic magma (Hibbard, 1991), but acicular apatites do not appear to be relict products of country-rock (Vernon, 1984). Thus the mafic enclaves were not likely the restite after partial melting processes. In addition, the compositional gap between mafic enclaves and host granodiorites (Fig. 4a) suggests that the granodiorites could not derived by fractional crystallization of mafic magmas, so the mafic enclaves cannot represent the accumulations of early formed crystals (Wang et al., 2012). Therefore it is reasonable to interpret the mafic enclaves as the products of mantle-derived magmas, which mixed with crust-derived felsic magmas, and then produce the whole granitoid's body.

The magma mixing processes can be testified by the following lines of evidence:

(1) The presence of MME and the coeval host granodiorites, indicates mixing of mafic and felsic magma (e.g., Vernon, 1990; Barbarin and Didier, 1992; Dong et al., 2005; Mo et al., 2005, 2007).
(2) As mentioned above from petrological observations, most of the MME have K-feldspar megacrysts and needle-like crystals of apatite (Fig. 2). The high content of ferromagnesian minerals in the MME (more than 50 vol.%) is supposed to the evidence of a cognate process (Donaire et al., 2005), because the mafic phases can nucleate more quickly than quartz and feldspar and can be enriched in early crystallization products (Weinberg et al., 2001). However, the MME in Mamba is not likely the case of the cognate process, but more likely to generate from a magma interaction process (Kaygusuz and Aydınçakır, 2009). This is also supported by the identical mineral between the MME and host rocks, since low rheological contrast between two magmas allows crystal transfer from the host magma into the basic magma (Barbarin and Didier, 1992; Waight et al., 2000; Perugini et al., 2003).
(3) Rock geochemistry hint two end-members in the mixing system. The mafic enclaves have gabbroic–dioritic compositions (low SiO_2, high MgO), and relative low Nb/U ratio (4.4–6.9) that is comparable to the continental crust (Nb/U = 6.2; Rudnick and Fountain, 1995). These imply that the mafic enclaves have both mantle and crustal signatures. The Mamba mafic samples that have low Ni (14–52 ppm) and Cr (13–156 ppm) content, also imply a modified mantle-derived magma by crustal component (Kelemen et al., 1998). Otherwise, the MME and host rocks have identical trace elements and isotopic compositions, but distinctive major elements, suggesting that magma mixing due to Sr–Nd isotopic equilibrium can be rapidly achieved between the mafic enclaves and their host rocks through time (Pin et al., 1990; Holden et al., 1991; Poli and Tommasini, 1991; Elburg, 1996). The isotopic equilibration of Sr is more rapid than Nd during the magma mixing processes (Holden et al., 1987; Lesher, 1990; Pin et al., 1990), therefore we can see that in Mamba samples, with a less varied change of Sr than that of Nd isotopes (Fig. 9).

The MME are high-K calc-alkaline to shoshonitic rocks (Fig. 5a). Such feature is significantly distinctive from the contemporaneous gabbroic rocks in southern Lhasa subterrane (K_2O = 0.85–1.06 wt.%; Fig. 5a), the latter were thought to be generated from the mantle wedge (Guan et al., 2011). Together with the enriched Nd–Hf isotopic feature ($\varepsilon_{Nd}(t) = -4.0$ to -3.6; $\varepsilon_{Hf}(t) = -4.0$ to 0.2), indicates that the mafic enclaves in Mamba derived from an enriched mantle source. Besides, mafic enclaves are enriched in LILE, depleted in Nb and Ta, have lower Nb/Ta ratios (13.7 to 16.1) than the primitive mantle (17.5 ± 2.0; Sun and McDonough, 1989), which implies that the magma source has been metasomatized by the fluid. Ultimately, we can explain the Sr–Nd isotopic component by using two end-members mixing (Fig. 9), one is the ancient lower crust, and the other is the enriched mantle source metasomatized by fluid which can be represented by Laguo Tso back-arc basin basalts (BABB; Wang et al., unpublished data). The mantle end-member applied in this study is different with the source regions for Milin hornblende gabbros in southern Lhasa subterrane (Fig. 9). As a result, the Mamba mafic enclaves were generated from fluid metasomatized mantle source.

5.2.2. Host granodiorite with adakitic affinities

The Mamba Late Cretaceous host granodiorites in this study and published data (Meng et al., 2010) are characterized by high Al_2O_3 (14.4–15.7 wt.%), Sr (680–766 ppm), Sr/Y (52.3–68.3), low Yb (0.95–1.27 ppm) and Y (10.8–14.5 ppm) and slightly negative Eu anomalies (δEu = 0.83–0.91), showing typical adakitic geochemical features (Defant and Drummond, 1990; Fig. 6). Due to their high SiO_2 content (66.2–68.5 wt.%), they also can be classified as high-silica adakites (HSA; Martin et al., 2005). Adakites were usually considered to be generated through crustal assimilation and fractional crystallization (AFC) of parental basaltic magmas (e.g., Castillo et al., 1999); partial melting of subducted oceanic crust (Defant and Drummond, 1990; Rapp et al., 1999; Gutscher et al., 2000; Martin et al., 2005; Wang et al., 2007; Zhu et al., 2009c); partial melting of mafic rocks in the lower part of a thickened crust (Atherton and Petford, 1993; Sheppard et al., 2001; Chung et al., 2003; Hou et al., 2004; Condie, 2005; Wang et al., 2005; Guan et al., 2012) and magma mixing (Guo et al., 2007; Xu et al., 2012). Due to the Mamba adakitic host granitoids and mafic enclaves that have different sources as discussed above, it excludes the granitic melts derived from the mafic melts through fractional crystallization. In addition, the absence of correlation between SiO_2 and most of the other major element oxide in Harker diagram (Fig. 5) exhibit that it differs from the basalt–rhyolite series generated through AFC process (Castillo et al., 1999). Besides, Mamba host granitoids and mafic enclaves have consistent Sr isotopic concentration (Fig. 9 and Table 3), indicating that they have not experienced significant crustal contamination. Thus, we preclude the possibility that the adakitic rocks were generated by crustal assimilation or fractional crystallization (AFC) of parental basaltic magmas and the shallow-level crustal contamination is not obvious.

The adakite generated by partial melting of subducted oceanic crust generally have high $Mg^{\#}$ (>50) or are similar to high-Mg andesites, since $Mg^{\#}$ values can be enhanced by the interaction with the mantle peridotite during magma ascent (e.g., Kay and Kay, 1993; Zhu et al., 2009c). Experimental research indicates that slab melt assimilating peridotite and undergoing metasomatic reactions involving orthopyroxene and garnet, during their ascent through the mantle wedge, and this process will significantly modify the SiO_2, MgO, Ni, and Cr contents (Rapp et al., 1999). As to Mamba adakitic granodiorites, although they have similar $Mg^{\#}$ (48–49) to the slab-derived adakites, their enriched whole-rock Sr–Nd and zircon Hf isotopic compositions ($(^{87}Sr/^{86}Sr)_i$ = 0.7066–0.7067, $\varepsilon_{Nd}(t) = -5.7$ to -4.1, $\varepsilon_{Hf}(t) = -7.5$ to -0.3; Figs. 9 and 10) and high K_2O contents (2.57–4.14 wt.%) are distinct from the rocks generated by partial melting of subducted oceanic crust (e.g. $(^{87}Sr/^{86}Sr)_i$ = 0.7041–0.7051, $\varepsilon_{Nd}(t)$ = 3.7–5.8, K_2O = 1.69–2.40 wt.%; Zhu et al., 2009c). The isotopic features of Mamba

Table 3
Bulk-rock geochemical data of the Mamba rocks.

Sample	MB14-4	MB16-1	MB17-1	MB13-2	MB13-2R	MB14-2	MB14-2R	MB14-5	MB13-3	MB12-1*	MB12-1R*	MB12-3*	MB12-5*	MB12-7*	MB12-8*	MB12-9*
Rock type	Granodiorite			Dioritic enclave					Gabbroic enclave	Granodiorite						
XRF—major element(wt.%)																
SiO_2	67.22	66.63	67.46	53.85	53.96	57.58		57.23	51.53	68.48		66.21	66.54	67.6	66.6	66.44
TiO_2	0.61	0.56	0.53	1.48	1.5	1.02		1.05	1.34	0.57		0.62	0.62	0.52	0.59	0.59
Al_2O_3	14.99	15.65	15.06	17.24	17.32	15		16.1	17.27	14.37		14.93	15.23	15.54	14.68	15.69
TFe_2O_3	4.07	3.7	3.61	8.71	8.72	7.72		6.43	9.5	3.71		3.95	4.13	3.36	3.95	3.82
MnO	0.08	0.07	0.07	0.14	0.14	0.17		0.15	0.18	0.07		0.07	0.07	0.06	0.07	0.07
MgO	1.89	1.71	1.68	3.71	3.72	4.67		4.44	5.25	1.76		1.87	1.93	1.55	1.9	1.83
CaO	3.87	3.51	3.45	5.34	5.34	6.41		5.68	5.72	3.43		3.24	2.85	3.65	2.91	3.85
Na_2O	4.14	4.18	3.87	4.74	4.75	4.08		3.94	4.39	3.8		3.63	3.96	4.14	3.95	4.12
K_2O	2.57	3.63	3.48	2.73	2.74	1.83		3.61	2.81	3.26		4.14	3.35	3.1	3.2	3.1
P_2O_5	0.27	0.28	0.25	0.66	0.67	0.4		0.46	0.5	0.26		0.28	0.3	0.23	0.28	0.26
LOI	0.37	0.32	0.63	1.59	1.55	0.77		0.5	1.06	0.4		0.93	1.28	0.36	2.13	0.46
TOTAL	100.08	100.24	100.09	100.19	100.41	99.65		99.59	99.55	100.11		99.87	100.3	100.1	100.26	100.23
A/CNK	0.9	0.91	0.92	0.84	0.84	0.74		0.78	0.83	0.9		0.91	0.99	0.92	0.96	0.91
$Mg^{\#}$	48	48	48	46	46	55		58	52	48		48	48	48	49	49
ICP-MS—trace element (ppm)																
Be	2.16	2.26	2.59			3.01	2.9	2.47	3.3	2.25	2.29	2.04	2.14	2.07	2.45	2.4
Sc	6.7	6.76	7.81			19.8	18.4	15.4	12.3	6.85	6.95	7.7	6.97	5.8	7.31	6.65
V	70.2	65.7	79.4			177	166	147	184	71.1	73.4	78.5	68.9	59.7	75.4	75
Cr	26.5	28.6	31.1			156	144	100	13	27.4	27.7	30.3	28.8	22.7	30.5	28.3
Co	8.98	8.13	9.61			21.3	19.9	20.3	21	8.88	8.97	9.65	9.22	7.3	9.84	9.29
Ni	12.5	12	14.1			36.5	34	51.6	13.8	12.3	13.4	13.5	12.5	10.2	14.1	13.1
Cu	2.74	3.54	2.96			10.5	9.63	6.55	28.1	3.31	3.51	3.03	2.66	3.03	2.9	2.62
Zn	59.2	49.1	59			106	98.5	97.8	119	53.8	54.3	59	54.8	45.9	59.2	57.4
Ga	19.9	18.9	20.7			23.4	21.9	22.1	28.9	19.6	20.1	20	19.1	18.8	19.9	21.5
Rb	144	133	117			123	117	194	199	133	135	154	121	115	136	101
Sr	738	680	755			627	588	555	576	725	736	758	742	746	738	766
Y	10.8	11.1	13			20	18.8	18.3	29	12.3	12.5	14.5	12	11.8	11.3	12.4
Zr	175	156	202			198	177	207	263	187	185	176	184	167	177	191
Nb	12.1	12.6	14.5			22.4	21.1	20.1	30.4	13.1	13.4	15.1	13	12.6	12.8	13.9

Cs	7.31	5.16	4.26	9.59	9.07	11.2	10.9	5.43	5.57	3.38	2.61	4.28	3.27	4.66
Ba	489	481	244	189	178	482	296	420	420	887	487	360	400	381
La	62.7	46.8	41.4	51.1	49.1	55.7	77.2	45	44.4	67.5	64.1	66.8	44	40.5
Ce	97.2	84.5	84	111	105	117	167	85.7	85.7	113	103	102	79.6	76
Pr	9.56	8.84	9.49	12.8	12.2	13.2	19.5	9.37	9.56	11.7	10.2	10.2	8.82	9.18
Nd	32	30.9	34	46.5	44.3	47.4	69.7	33.1	33.7	40.9	34.6	34.4	30.9	32.7
Sm	4.77	4.71	5.48	7.87	7.47	7.76	11.1	5.27	5.43	6.24	5.24	5.24	4.87	5.23
Eu	1.21	1.18	1.38	1.92	1.84	2.16	2.68	1.36	1.34	1.54	1.26	1.3	1.21	1.38
Gd	3.33	3.41	3.84	5.92	5.62	5.65	8.38	3.82	3.87	4.53	3.71	3.63	3.52	3.79
Tb	0.42	0.43	0.49	0.76	0.72	0.71	1.07	0.47	0.47	0.55	0.47	0.45	0.44	0.47
Dy	2.12	2.15	2.5	3.81	3.64	3.57	5.5	2.35	2.48	2.78	2.28	2.33	2.2	2.48
Ho	0.38	0.4	0.45	0.7	0.69	0.67	1.03	0.44	0.45	0.52	0.43	0.42	0.41	0.45
Er	1.03	1.02	1.24	1.88	1.8	1.74	2.79	1.16	1.19	1.4	1.15	1.12	1.07	1.18
Tm	0.15	0.15	0.18	0.26	0.25	0.24	0.39	0.17	0.17	0.19	0.16	0.15	0.15	0.16
Yb	0.95	1	1.23	1.8	1.67	1.58	2.64	1.07	1.13	1.27	1.05	1.03	0.99	1.15
Lu	0.15	0.16	0.18	0.28	0.26	0.24	0.41	0.16	0.17	0.18	0.17	0.15	0.16	0.18
Hf	4.28	3.97	5.14	5.06	4.6	5.03	6.64	4.63	4.61	4.41	4.58	4.22	4.41	4.68
Ta	0.82	0.89	1.02	1.61	1.54	1.25	2.21	0.93	0.96	1.1	0.9	0.94	0.86	0.96
Pb	19.5	19.1	16.4	14.2	13.5	21.4	18	18	18.3	20.4	16.3	17.7	17.3	18
Th	21.6	19.8	14.9	12.9	12.7	13.1	19.1	26.9	26.2	25.2	32.4	21	22.9	22.6
U	2.97	2.53	2.87	4.52	4.04	2.92	6.89	3.11	3.29	3.83	3.67	3.02	4.16	3.04
Sr/Y	68.3	61.2	58.1	31.3	31.4	30.2	19.9	59	58.8	52.3	61.8	63.1	65.2	61.6
$^{87}Rb/^{86}Sr$	0.5829	0.5853		0.5861			1.0306	0.5489		0.604			0.55	
$^{87}Sr/^{86}Sr$	0.70743	0.70732		0.707376			0.708505	0.707408		0.70746			0.707398	
$\pm 2\sigma$	0.000005	0.000007		0.000006			0.000005	0.000006		0.000005			0.000006	
$(^{87}Sr/^{86}Sr)_i$	0.70673	0.70662		0.706668			0.70726	0.706722		0.706705			0.70671	
$^{147}Sm/^{144}Nd$	0.0902	0.0923		0.1022			0.096	0.0964		0.0922			0.0952	
$^{143}Nd/^{144}Nd$	0.51236	0.51229		0.512401			0.512377	0.512372		0.512359			0.512357	
$\pm 2\sigma$	0.000009	0.000026		0.000005			0.000008	0.000007		0.000005			0.000003	
$(^{143}Nd/^{144}Nd)_i$	0.51231	0.51224		0.512344			0.512324	0.512317		0.512306			0.512302	
$\varepsilon_{Nd}(t)$	−4.4	−5.7		−3.6			−4	−4.1		−4.3			−4.3	
T_{DM}(Ga)	0.98	1.08		1.02			1	1.01		0.99			1.02	

Samples MB12-1* quoted from Meng et al. (2010). LOI = loss on ignition. Mg# = 100 × Mg^{2+} / (Mg^{2+} + TFe^{2+}), TFeO* = 0.9 × TFe_2O_3. Corrected formula as follows: $(^{87}Sr/^{86}Sr)_i = (^{87}Sr/^{86}Sr)_{sample} - {}^{87}Rb/^{86}Sr\,(e^{\lambda t} - 1)$, $\lambda = 1.42 \times 10^{-11}\ a^{-1}$; $(^{143}Nd/^{144}Nd)_i = (^{143}Nd/^{144}Nd)_{sample} - (^{147}Sm/^{144}Nd)_m \times (e^{\lambda t} - 1)$, $\varepsilon_{Nd(t)} = [(^{143}Nd/^{144}Nd)_{sample}/(^{143}Nd/^{144}Nd)_{CHUR}(t) - 1] \times 10^4$, $(^{143}Nd/^{144}Nd)_{CHUR}(t) = 0.512638 - 0.1967 \times (e^{\lambda t} - 1)$. $T_{DM} = 1 / \lambda \times \ln\ \{1 + [((^{143}Nd/^{144}Nd)_{Sample} - 0.51315) / ((^{147}Sm/^{144}Nd)_{Sample} - 0.21317)]\}$, $\lambda_{Sm-Nd} = 6.54 \times 10^{-12}\ a^{-1}$; T_{DM2} is the two-stage Nd depleted-mantle model age calculated using the same assumption formulation as Keto and Jacobsen (1987).

Table 4
Zircon Hf isotopic data for the Late Cretaceous Mamba granodiorite and enclaves.

No.	Age (Ma)	$^{176}Yb/^{177}Hf$	$^{176}Lu/^{177}Hf$	$^{176}Hf/^{177}Hf$	2σ	$^{176}Hf/^{177}Hf_i$	$\varepsilon_{Hf}(0)$	$\varepsilon_{Hf}(t)$	T_{DM} (Ma)	T^C_{DM}(Ma)	$f_{Lu/Hf}$
MB14-4, host granite, 83.7 ± 0.5 Ma, $\varepsilon_{Hf}(t)$ = −7.5 – −0.3 (18 analyses)											
1	83	0.009326	0.000466	0.282673	0.000015	0.282672	−3.5	−2.1	808	1250	−0.99
2	84	0.011606	0.000589	0.282636	0.000017	0.282635	−4.8	−3.4	863	1333	−0.98
3	84	0.014499	0.000724	0.282649	0.000021	0.282648	−4.3	−3.0	847	1304	−0.98
4	83	0.017468	0.000877	0.282725	0.000018	0.282724	−1.7	−0.3	744	1135	−0.97
5	83	0.018390	0.000926	0.282667	0.000022	0.282665	−3.7	−2.4	827	1266	−0.97
6	84	0.008039	0.000407	0.282631	0.000022	0.282630	−5.0	−3.6	866	1343	−0.99
7	84	0.014208	0.000728	0.282639	0.000020	0.282638	−4.7	−3.3	862	1327	−0.98
8	83	0.012538	0.000643	0.282609	0.000020	0.282608	−5.8	−4.4	902	1395	−0.98
9	84	0.017233	0.000854	0.282632	0.000018	0.282630	−5.0	−3.6	875	1344	−0.97
10	85	0.016009	0.000814	0.282668	0.000016	0.282667	−3.7	−2.3	823	1261	−0.98
11	84	0.019530	0.000924	0.282522	0.000022	0.282521	−8.8	−7.5	1030	1588	−0.97
12	84	0.015059	0.000739	0.282655	0.000019	0.282654	−4.1	−2.8	840	1291	−0.98
13	84	0.014721	0.000749	0.282624	0.000018	0.282623	−5.2	−3.9	884	1361	−0.98
14	84	0.011704	0.000588	0.282666	0.000022	0.282665	−3.7	−2.4	821	1265	−0.98
15	83	0.016074	0.000812	0.282663	0.000025	0.282661	−3.9	−2.5	831	1275	−0.98
16	84	0.013869	0.000685	0.282654	0.000026	0.282653	−4.2	−2.8	839	1292	−0.98
17	84	0.012710	0.000601	0.282620	0.000019	0.282619	−5.4	−4.0	885	1369	−0.98
18	84	0.014550	0.000733	0.282622	0.000020	0.282621	−5.3	−3.9	885	1364	−0.98
MB14-2, dioritic enclave, 85.2 ± 0.4 Ma, $\varepsilon_{Hf}(t)$ = −4.0 – 0.2 (17 analyses)											
1	85	0.019216	0.000939	0.282637	0.000014	0.282636	−4.8	−3.4	869	1330	−0.97
2	84	0.011587	0.000575	0.282670	0.000016	0.282669	−3.6	−2.2	815	1257	−0.98
3	86	0.008818	0.000439	0.282631	0.000018	0.282630	−5.0	−3.6	867	1343	−0.99
4	85	0.015616	0.000689	0.282630	0.000020	0.282629	−5.0	−3.6	874	1346	−0.98
5	86	0.048862	0.002061	0.282726	0.000017	0.282723	−1.6	−0.3	767	1135	−0.94
6	84	0.029150	0.001256	0.282636	0.000030	0.282634	−4.8	−3.5	878	1335	−0.96
7	87	0.016651	0.000812	0.282632	0.000016	0.282631	−4.9	−3.5	873	1340	−0.98
8	86	0.008896	0.000450	0.282622	0.000016	0.282621	−5.3	−3.9	879	1363	−0.99
9	86	0.015716	0.000794	0.282726	0.000024	0.282725	−1.6	−0.2	741	1130	−0.98
10	85	0.017075	0.000853	0.282619	0.000020	0.282618	−5.4	−4.0	892	1371	−0.97
12	85	0.023918	0.001119	0.282738	0.000021	0.282736	−1.2	0.2	731	1106	−0.97
13	85	0.012774	0.000632	0.282628	0.000018	0.282627	−5.1	−3.7	875	1351	−0.98
14	84	0.015990	0.000777	0.282644	0.000014	0.282643	−4.5	−3.2	856	1316	−0.98
15	85	0.020836	0.001003	0.282712	0.000025	0.282710	−2.1	−0.8	765	1164	−0.97
16	85	0.011478	0.000585	0.282655	0.000020	0.282654	−4.1	−2.7	836	1290	−0.98
17	83	0.011690	0.000547	0.282637	0.000014	0.282636	−4.8	−3.4	861	1332	−0.98
18	86	0.021445	0.001023	0.282726	0.000017	0.282725	−1.6	−0.2	745	1132	−0.97

$\varepsilon_{Hf(t)} = 10{,}000 \times \{[(^{176}Hf/^{177}Hf)_S - (^{176}Lu/^{177}Hf)_S \times (e^{\lambda t} - 1)] / [(^{176}Hf/^{177}Hf)_{CHUR,0} - (^{176}Lu/^{177}Hf)_{CHUR} \times (e^{\lambda t} - 1)] - 1\}$.
$T_{DM} = 1 / \lambda \times \ln\{1 + [(^{176}Hf/^{177}Hf)_S - (^{176}Hf/^{177}Hf)_{DM}] / [(^{176}Lu/^{177}Hf)_S - (^{176}Lu/^{177}Hf)_{DM}]\}$.
$T^C_{DM} = T_{DM} - (T_{DM} - t) \times [(f_{cc} - f_s) / (f_{cc} - f_{DM})]$.
$f_{Lu/Hf} = (^{176}Lu/^{177}Hf)_S / (^{176}Lu/^{177}Hf)_{CHUR} - 1$.
where, $\lambda = 1.867 \times 10^{-11}$ year^{-1} (Söderlund et al., 2004); $(^{176}Lu/^{177}Hf)_S$ and $(^{176}Hf/^{177}Hf)_S$ are the measured values of the samples; $(^{176}Lu/^{177}Hf)_{CHUR} = 0.0336$ and $(^{176}Hf/^{177}Hf)_{CHUR,0} = 0.282785$ (Bouvier et al., 2008); $(^{176}Lu/^{177}Hf)_{DM} = 0.0384$ and $(^{176}Hf/^{177}Hf)_{DM} = 0.28325$ (Griffin et al., 2000); $(^{176}Lu/^{177}Hf)_{mean\ crust} = 0.015$; $f_{cc} = [(^{176}Lu/^{177}Hf)_{mean\ crust} / (^{176}Lu/^{177}Hf)_{CHUR}] - 1$; $f_s = f_{Lu/Hf}$; $f_{DM} = [(^{176}Lu/^{177}Hf)_{DM} / (^{176}Lu/^{177}Hf)_{CHUR}] - 1$; t = crystallization time of zircon.

adakitic granodiorites also differ from the ancient lower crust in central Lhasa subterrane assumed by Miller et al. (1999) ($\varepsilon_{Nd}(t) = -22$). According to Zhu et al. (2011a), central Lhasa subterrane was once a microcontinent with Archean basement with much negative $\varepsilon_{Hf}(t)$. Therefore, partial melting of ancient lower crust alone cannot explain the isotopic signature of Mamba adakitic rocks. In combination with the presence of coeval mafic enclaves and significant wider change in zircon $\varepsilon_{Hf}(t)$ from the older rocks to the 85 Ma rocks (our unpublished data; Fig. 10), suggest the involvement of extensive mantle-derived melt in the petrogenesis of the host granodiorites.

As mentioned above, Mamba host adakitic granodiorites and MME have similar trace elements and isotopic compositions attributed to the magma mixing. Sr–Nd two end-member mixing modeling of the granodiorites shows clear trend of mixing between the ancient lower crust and the Laguo Tso back-arc basin basalts (Fig. 9). The lower crust in Mamba, central Lhasa subterrane could be a thickened lower crust, together with the recognition of significant shortening from other studies (Yin et al., 1988; Leier et al., 2007; Wen et al., 2008b) and the presence of adakitic rocks further indicates that crustal thickening had previously occurred in the central Lhasa subterrane before ca. 85 Ma.

The Mamba host granodiorites may generate from magma mixing between partial melt of ancient thickened lower crust and the enriched mantle source metasomatized by fluid during ascent. Mantle-derived magmas emplaced within lower crust provide enough heat to enhance crustal anatexis and they are injected into and mix with the crustal-derived melt which is similar to the result from Quxu pluton in southern Lhasa subterrane (Dong et al., 2005; Mo et al., 2005).

5.3. Geodynamic interpretation

The geodynamic mechanism of Late Cretaceous magmatism in southern and central Lhasa subterranes has been an issue of hot debate, including Neo-Tethyan low-angle or flat-slab subduction (Coulon et al., 1986; Ding et al., 2003; Wen et al., 2008a), Neo-Tethyan subduction at a relatively steep angle (Jiang et al., 2012) and Neo-Tethyan mid-ocean ridge subduction (Zhang et al., 2010a, 2011; Zhu et al., 2011a). The presence of large-scale Cretaceous magmatism (Zhu et al., 2008a,b, 2009c, 2011a), especially the mafic magmatism (88 Ma) observed in southern Lhasa subterrane (Guan et al., 2011) cannot be interpreted as the low-angle or flat-slab model. Considering the model of Neo-Tethyan subduction at a relatively steep angle, it is difficult to interpret the existence of 90 Ma high temperature condition and low H_2O activity charnockite (Zhang et al., 2010a) as well as the intense 90–80 Ma igneous rocks obtained in southern Lhasa subterrane (e.g., Guan et al., 2011). That is, the normal Neo-Tethyan subduction model is not coincidence with the extreme high heat. Relating to the Neo-Tethyan mid-ocean ridge subduction, which was firstly proposed by Zhang et al. (2010a), is result from the presence of high temperature condition and low H_2O activity

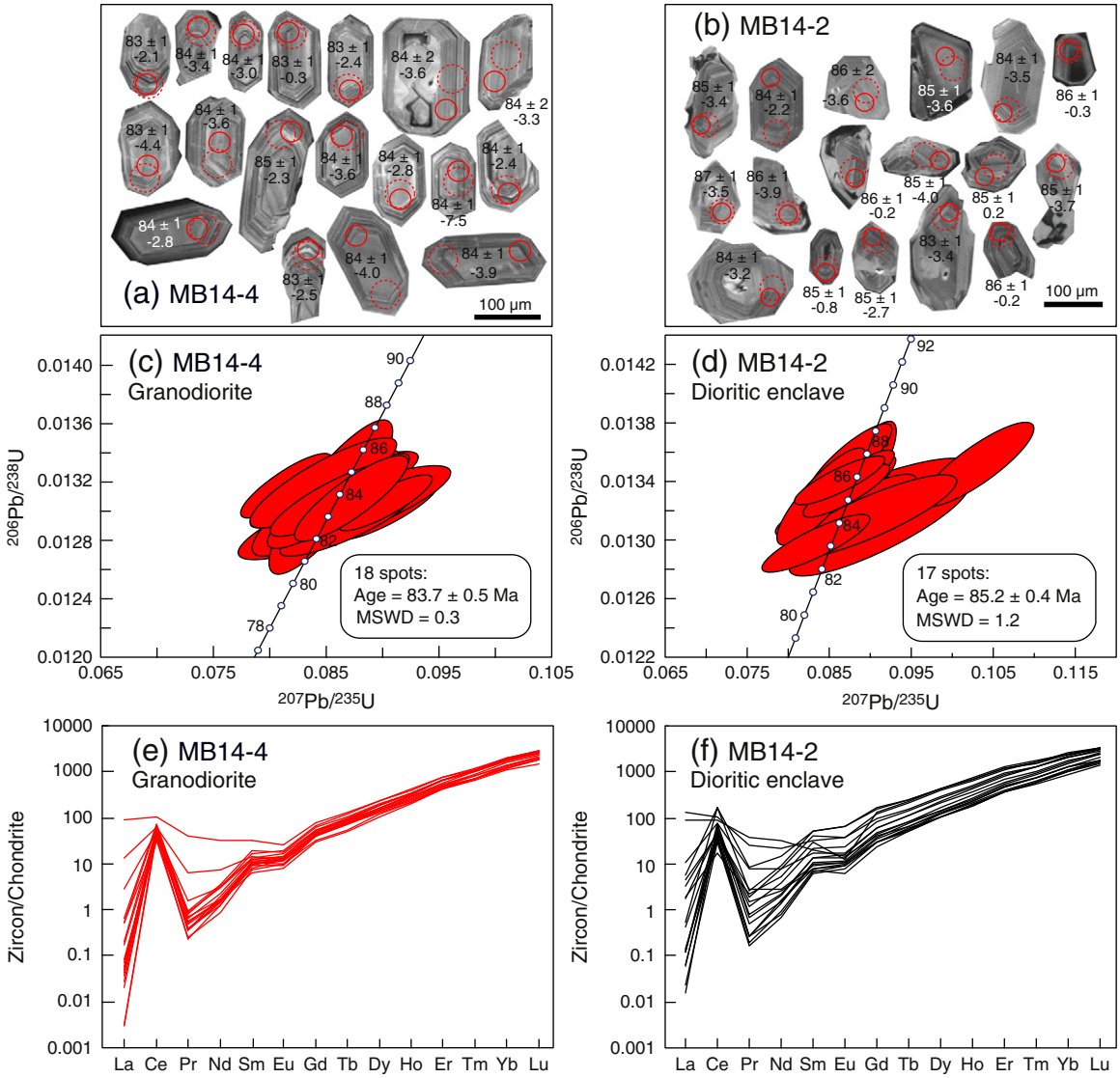

Fig. 3. Cathodoluminescence (CL) images (a–b), concordia diagrams (c–d), and chondrite-normalized REE patterns (e–f) for zircons of the igneous rocks in Mamba. Solid and dashed circles indicate the locations of LA–ICP-MS U–Pb dating and Hf analyses, respectively. Zircon U–Pb ages and $\varepsilon_{Hf}(t)$ values are given for each analyses.

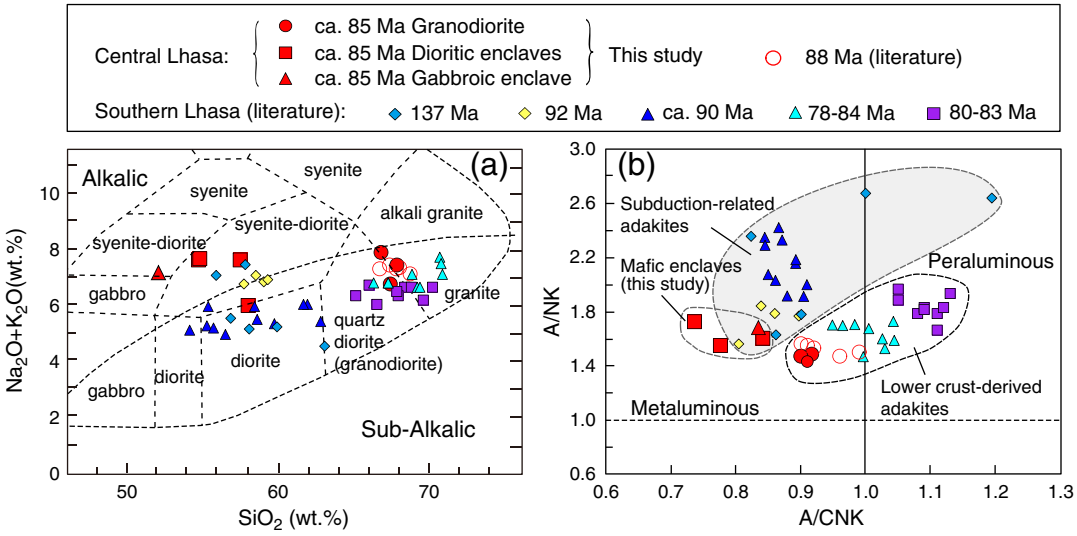

Fig. 4. (a) Total alkalis vs. silica diagram (Wilson, 1989); (b) A/NK vs. A/CNK diagram (Maniar and Piccoli, 1989) showing sample compositional variation. Data sources: Central Lhasa: 88 Ma (Meng et al., 2010); Southern Lhasa: 137 Ma (Zhu et al., 2009c); 92 Ma (Jiang et al., 2012); 90 Ma (Zhang et al., 2010a); 78–84 Ma (Guan et al., 2010); 80–83 Ma (Wen et al., 2008a).

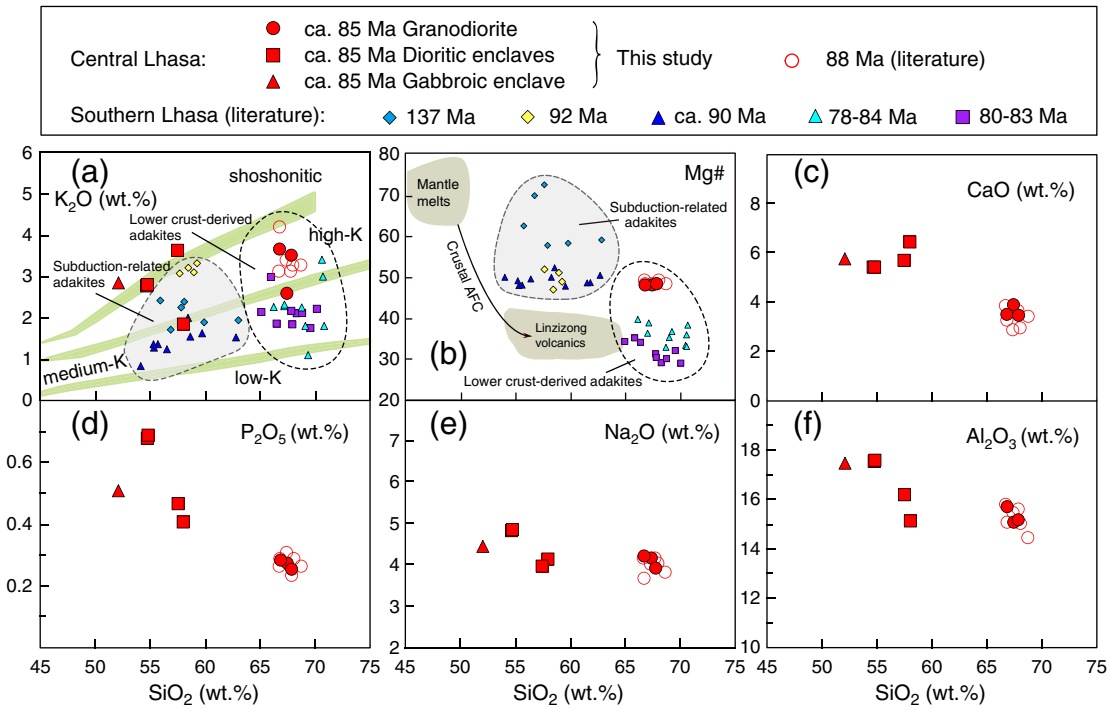

Fig. 5. Co-variations of K_2O, Mg#, CaO, P_2O_5, Na_2O and Al_2O_3 vs. SiO_2 for the Mamba igneous rocks. SiO_2 vs. K_2O is from Le Maitre (2002). Data sources are as in Fig. 4.

charnockite, along with the research of the high density carbonic fluids in the slab window (Zhang et al., 2011). Was Mamba contemporary magmatism the direct products of the Neo-Tethyan mid-ocean ridge subduction?

Mamba currently locates more than 100 km north of the former trench which is now represented by the Yalung Zangbo suture zone (IYZSZ, Fig. 1). If the major upper crustal shortening have taken place in this area during 80–70 Ma was taken into account (>40%, Leier et al., 2007; Wen et al., 2008b), which can be seen in the study area by the cross-section of the upper Cretaceous and older rock units strongly deformed and unconformable overlain by the gently folded Linzizong volcanic succession (Burg et al., 1983; Allègre et al., 1984; Coward et al., 1988; He et al., 2007); when the Mamba pluton emplaced (ca. 85 Ma), it possibly lied over ~200 km from the suture in southern Lhasa subterrane. With such a long distance, mid-ocean ridge subduction model cannot be applied in explaining the Mamba intrusives. The similar evidence will also preclude the possibility that Mamba intrusive was the products of the post-collision extension between Lhasa and Qiangtang terranes after they collided at about 145 Ma (e.g., Zhu et al., 2011a).

Consequently, we propose that Mamba granitoids were more likely generated in a back-arc extension environment with the following evidences: (1) Based on the research of the neighboring sedimentary basins, the sediment of the Upper Cretaceous Takena Formation mainly derived from pre-existed Gangdese volcanic arc, and most consistent with deposition in a back-arc setting (e.g., Leier et al., 2007). The existence of Upper Cretaceous Takena Formation, which was also named Shexing Formation, in the southwest of Mamba (Fig. 1b), indicates that Mamba Late Cretaceous magmatism should generate in the same back-arc tectonic settings. (2) Geochemically, the gabbroic enclave in this study is high K_2O, shoshonitic rock, which is distinct from the coeval middle-K calc-alkaline gabbroic rocks in southern Lhasa subterrane. (3) Tectonically, the gabbroic enclave has high Zr content (263 ppm) and Zr/Y ratio (Zr/Y = 9), which has the affinity of within-plate basaltic rocks (Zhao et al., 2011; Fig. 7), instead of the typical arc basaltic rocks

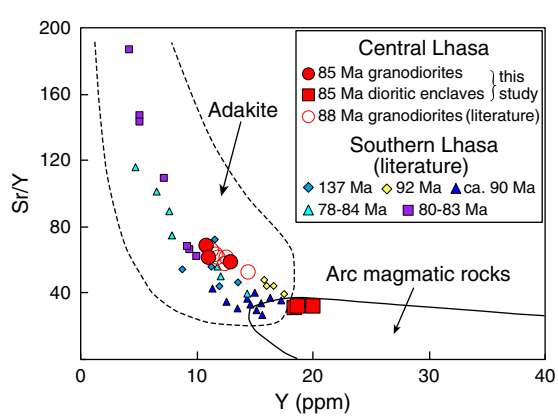

Fig. 6. Sr/Y vs. Y discrimination diagram showing data for adakites and normal calc-alkaline rocks (Defant and Drummond, 1990). Data sources are as in Fig. 4.

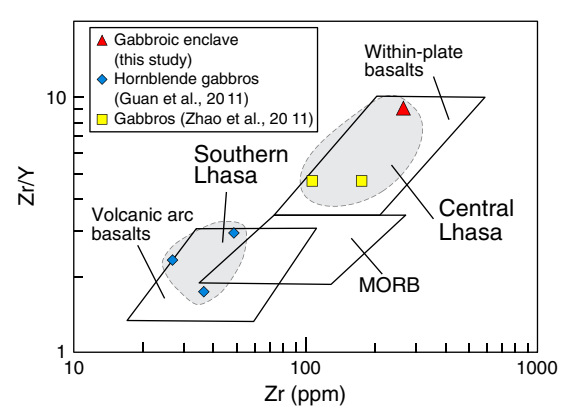

Fig. 7. Zr/Y–Zr discrimination diagram (Pearce and Norry, 1979): MORB = mid-ocean ridge basalts. Data sources: hornblende gabbros (Guan et al., 2011); gabbros (Zhao et al., 2011).

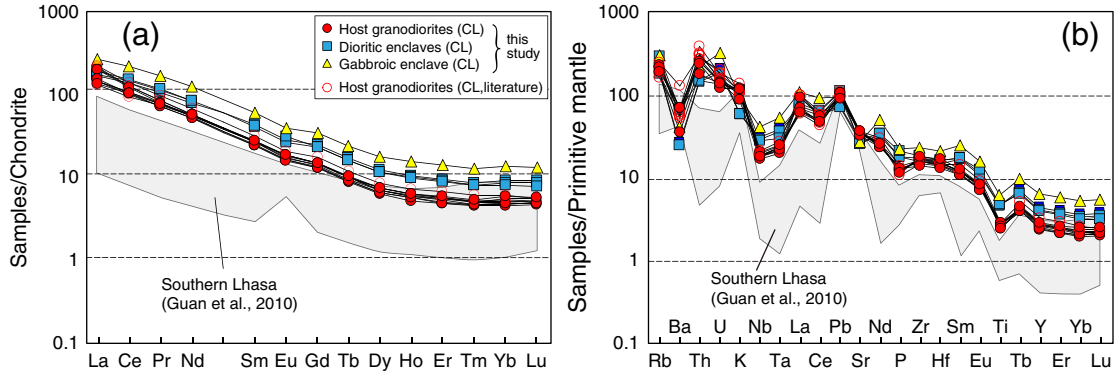

Fig. 8. Chondrite-normalized REE and primitive-mantle-normalized trace element patterns for the igneous rocks in Mamba, central Lhasa subterrane. Data for normalization and plotting are from Boynton (1984) and Sun and McDonough (1989), respectively. Coeval granitoids rocks (Guan et al., 2010) are shown for comparison.

(e.g., Guan et al., 2011; Fig. 7), (4) Synchronous bimodal igneous occurred in Coqen (Qu et al., 2006) and Namling (Ye, 2013) further supports that Late Cretaceous magmatism in central Lhasa subterrane generated in an extensional setting.

In summary, these evidences allow the inference that the ~85 Ma magmatism in Mamba, central Lhasa subterrane, probably the products of back-arc extension of Neo-Tethyan Ocean (Fig. 11). Under this geodynamic regime, Neo-Tethyan mid-ocean ridge subduction only affected the Late Cretaceous magmatism in southern Lhasa subterrane. Due to the gravity of the subducting slab, a roll-back of the slab may occur and result in the formation of the extensional environment after the subduction zone. During this process, the upwelling mantle-derived magmas provide not only materials but also enough heat supply that could induce melting of the enriched lithospheric mantle and mafic lower crust to generate the ~85 Ma Mamba adakitic host granodiorite, gabbroic enclave, and dioritic enclaves.

6. Conclusions

(1) The Mamba host granodiorites and mafic enclaves in central Lhasa subterrane were contemporaneously emplaced in Late Cretaceous (~85 Ma).

(2) Mamba host granodiorites, gabbroic and dioritic enclaves, are high-K to shoshonitic metaluminous rocks, with enrichment of LILEs and depletion of HFSEs. The host granodiorites are high Sr, Sr/Y, low Y adakitic rocks.

(3) Mamba adakitic host granodiorites and mafic enclaves may derive from magma mixing between the melts from ancient thickened lower crust and enriched fluid-metasomatized mantle source, in a back-arc extensional environment.

Acknowledgments

This research was financially co-supported by the National Key Project for Basic Research of China (Projects 2009CB421002 and 2011CB403102), the Strategic Priority Research Program (B) of the Chinese Academy of Sciences (XDB03010301), National Natural Science Foundation of China (41225006, 41273044, 41073013, 40830317, and 40973026), the IGCP project (IGCP/SIDA-600), the Fundamental Research Funds for the Central Universities (2010ZD02), the New Century Excellent Talents in University (NCET-10-0711), the Chinese 111 Project (B07011), the Program for Changjiang Scholars and Innovative Research Team in the University of Ministry of Education of China (PCIRT1083), and the Program of the China Geological Survey (1212011121260 and 1212011121066), and NSF (EAR1111959, 1111586). Min Liu is thanked for her help with some zircon and rock geochemical analyses. We thank Zhengfu Guo and anonymous reviewer for constructive comments and Editor M. Santosh for comments and editorial handling.

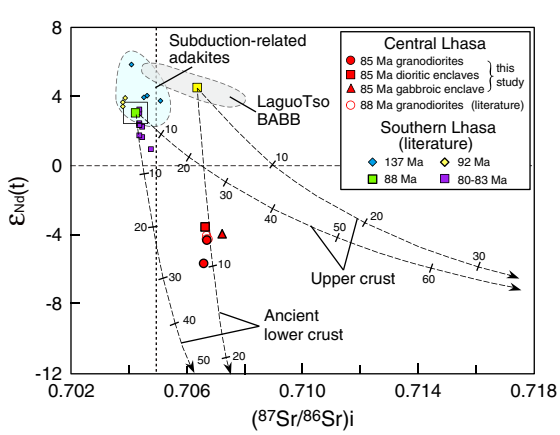

Fig. 9. $\varepsilon_{Nd}(t)$ vs. initial $^{87}Sr/^{86}Sr$ values diagram for the Mamba igneous rocks. Data sources: Central Lhasa: 88 Ma (Meng et al., 2010); Southern Lhasa: 137 Ma (Zhu et al., 2009c); 92 Ma (Jiang et al., 2012); 88 Ma (Guan et al., 2011); 80–83 Ma (Wen et al., 2008a); Ancient lower crust (Miller et al., 1999); Upper crust (Liu et al., 2006).

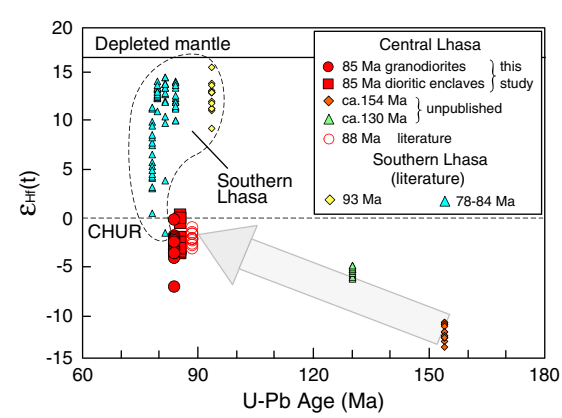

Fig. 10. $\varepsilon_{Hf}(t)$ vs. U–Pb age plot for the Mamba igneous rocks. Data sources: 154 Ma and 130 Ma (our unpublished data); 88 Ma (Meng et al., 2010); 92 Ma (Jiang et al., 2012); 78–84 Ma (Guan et al., 2010).

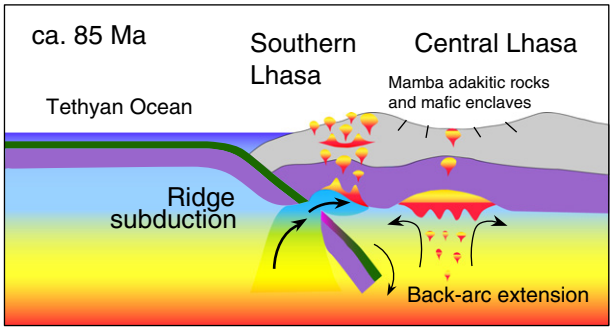

Fig. 11. Cartoon showing the tectonic setting of the Mamba ~85 Ma magmatism in the Lhasa Terrane, Tibet (modified from Zhu et al., 2013).

References

Allègre, C.J., Courtillot, V., Tapponnier, P., Hirn, A., Mattauer, M., Coulon, C., Jaeger, J.J., Achache, J., Schärer, U., Marcoux, J., 1984. Structure and evolution of the Himalaya–Tibet orogenic belt. Nature 307, 17–22.

Andersen, T., 2002. Correction of common lead in U–Pb analyses that do not report Pb-204. Chemical Geology 192, 59–79.

Atherton, M.P., Petford, N., 1993. Generation of sodium-rich magmas from newly underplated basaltic crust. Nature 362, 144–146.

Bacon, C.R., 1986. Magmatic inclusions in silicic and intermediate volcanic rocks. Journal of Geophysical Research 91, 6091–6112.

Barbarin, B., 2005. Mafic magmatic enclaves and mafic rocks associated with somegranitoids of the central Sierra Nevada batholith, California: nature, origin, and relations with the hosts. Lithos 88, 155–177.

Barbarin, B., Didier, J., 1992. Genesis and evolution of mafic microgranular enclaves through various types of interaction between coexisting felsic and mafic magmas. Transactions of the Royal Society of Edinburgh: Earth Sciences 83, 145–153.

Bonin, B., 1991. The enclaves of alkaline anorogenic granites: an overview. In: Didier, J., Barbarin, B. (Eds.), Enclaves and Granite Petrology. Developments in Petrology, 13. Elsevier, Amsterdam, pp. 179–189.

Bouvier, A., Vervoort, J.D., Patchett, P.J., 2008. The Lu–Hf and Sm–Nd isotopic composition of CHUR: constraints from unequilibrated chondrites and implications for the bulk composition of terrestrial planets. Earth and Planetary Science Letters 273, 48–57.

Boynton, W.V., 1984. Geochemistry of the rare earth elements: meteorite studies. In: Henderson, P. (Ed.), Rare Earth Element Geochemistry. Elsevier, pp. 63–114.

Burg, J.P., Proust, F., Tapponnier, P., Ming, C.G., 1983. Deformation phases and tectonic evolution of the Lhasa Block (Southern Tibet, China). Eclogae Geologicae Helvetiae 76, 643–665.

Castillo, P.R., Janney, P.E., Solidum, R.U., 1999. Petrology and geochemistry of Camiguin Island, southern Philippines: insights to the source of adakites and other lavas in a complex arc setting. Contributions to Mineralogy and Petrology 134, 33–51.

Chappell, B., White, A., Wyborn, D., 1987. The importance of residual source material (restite) in granite petrogenesis. Journal of Petrology 28, 1111–1138.

Chung, S.L., Liu, D.Y., Ji, J.Q., Chu, M.F., Lee, H.Y., Wen, D.J., Lo, C.H., Lee, T.Y., Qian, Q., Zhang, Q., 2003. Adakites from continental collision zones: melting of thickened lower crust beneath southern Tibet. Geology 31, 1021–1024.

Chung, S.L., Chu, M.F., Zhang, Y.Q., Xie, Y.W., Lo, C.H., Lee, T.Y., Lan, C.Y., Li, X.H., Zhang, Q., Wang, Y.Z., 2005. Tibetan tectonic evolution inferred from spatial and temporal variations in post-collisional magmatism. Earth-Science Reviews 68, 173–196.

Condie, K.C., 2005. TTGs and adakites: are they both slab melts? Lithos 80, 33–44.

Coulon, C., Maluski, H., Bollinger, C., Wang, S., 1986. Mesozoic and Cenozoic volcanic-rocks from central and southern Tibet: $^{39}Ar/^{40}Ar$ dating, petrological characteristics and geodynamical significance. Earth and Planetary Science Letters 79, 281–302.

Coward, M., Kidd, W., Yun, P., Shackleton, R., Hu, Z., 1988. The structure of the 1985 Tibet geotraverse, Lhasa to Golmud. Philosophical Transactions of the Royal Society of London. Series A, Mathematical and Physical Sciences 307–333.

Defant, M.J., Drummond, M.S., 1990. Derivation of some modern arc magmas by melting of young subducted lithosphere. Nature 347, 662–665.

Dewey, J.F., Shackleton, R.M., Chengfa, C., Yiyin, S., 1988. The tectonic evolution of the Tibetan Plateau. Philosophical Transactions of the Royal Society of London. Series A, Mathematical and Physical Sciences 327, 379–413.

Ding, L., Kapp, P., Zhong, D.L., Deng, W.M., 2003. Cenozoic volcanism in Tibet: evidence for a transition from oceanic to continental subduction. Journal of Petrology 44, 1833–1865.

Donaire, T., Pascual, E., Pin, C., Duthou, J.L., 2005. Micro-granular enclaves as evidence of rapid cooling in granitoid rocks: the case of the Los Pedroches granodiorite, Iberian Massif, Spain. Contributions to Mineralogy and Petrology 149, 247–265.

Dong, G.C., Mo, X.X., Zhao, Z.D., Guo, T.Y., Wang, L.L., Chen, T., 2005. Geochronologic constraints by SHRIMP II zircon U–Pb dating on magma underplating in the Gangdise Belt following India–Eurasia collision. Acta Geologica Sinica 79, 787–794.

Dong, G.C., Mo, X.X., Zhao, Z.D., Zhu, D.C., Wang, L.L., Chen, T., Li, B., 2006. Magma mixing in middle part of Gangdise magma belt: evidence from granitoid complex. Acta Petrologica Sinica 22, 835–844 (Chinese with English abstract).

Dong, X., Zhang, Z.M., Santosh, M., Wang, W., Yu, F., Liu, F., 2011a. Late Neoproterozoic thermal events in the northern Lhasa terrane, south Tibet: zircon chronology and tectonic implications. Journal of Geodynamics 52, 389–405.

Dong, X., Zhang, Z.M., Liu, F., Wang, W., Yu, F., Shen, K., 2011b. Zircon U–Pb geochronology of the Nyainqêntanglha Group from the Lhasa terrane: new constraints on the Triassic orogeny of the south Tibet. Journal of Asian Earth Sciences 42, 732–739.

Elburg, M.A., 1996. U–Pb ages and morphologies of zircon in microgranitoid enclaves and peraluminous host granite: evidence for magma mingling. Contributions to Mineralogy and Petrology 123, 177–189.

Gao, S.B., Zheng, Y.Y., Xie, M.C., Zhang, Z., Yan, X.X., Wu, B., Luo, J.J., 2011. Geodynamic setting and mieralizational implication of the Xueru intrusion in Ban'ge, Tibet. Earth Science-Journal of China University of Geosciences 36, 729–739 (in Chinese with English abstract).

Girardeau, J., Mercier, J.C.C., Xibin, W., 1985. Petrology of the mafic rocks of the Xigaze ophiolite, Tibet. Contributions to Mineralogy and Petrology 90, 309–321.

Griffin, W.L., Pearson, N., Belousova, E., Jackson, S., Van Achterbergh, E., O'Reilly, S.Y., Shee, S., 2000. The Hf isotope composition of cratonic mantle: LAM–MC–ICPMS analysis of zircon megacrysts in kimberlites. Geochimica et Cosmochimica Acta 64, 133–147.

Griffin, W.L., Wang, X., Jackson, S.E., Pearson, N.J., O'Reilly, S.Y., Xu, X.S., Zhou, X.M., 2002. Zircon chemistry and magma mixing, SE China: in-situ analysis of Hf isotopes, Tonglu and Pingtan igneous complexes. Lithos 61, 237–269.

Guan, Q., Zhu, D.C., Zhao, Z.D., Zhang, L.L., Liu, M., Li, X.W., Yu, F., Liu, M.H., Mo, X.X., 2010. Late Cretaceous adakites from the eastern segment of the Gangdese Belt, Southern Tibet: products of Neo-Tethyan mid-ocean ridge subduction. Acta Petrologica Sinica 26, 2165–2179 (in Chinese with English abstract).

Guan, Q., Zhu, D.C., Zhao, Z.D., Dong, G.C., Mo, X.X., Liu, Y.S., Hu, Z.C., Yuan, H.L., 2011. Zircon U–Pb chronology, geochemistry of the Late Cretaceous mafic magmatism in the southern Lhasa Terrane and its implications. Acta Petrologica Sinica 27, 2083–2094 (Chinese with English abstract).

Guan, Q., Zhu, D.C., Zhao, Z.D., Dong, G.C., Zhang, L.L., Li, X.W., Liu, M., Mo, X.X., Liu, Y.S., Yuan, H.L., 2012. Crustal thickening prior to 38 Ma in southern Tibet: evidence from lower crust-derived adakitic magmatism in the Gangdese Batholith. Gondwana Research 21, 88–99.

Guo, F., Nakamuru, E., Fan, W.M., Kobayoshi, K., Li, C.W., 2007. Generation of Palaeocene adakitic andesites by magma mixing; Yanji area, NE China. Journal of Petrology 48, 661–692.

Gutscher, M.A., Maury, R., Eissen, J.P., 2000. Can slab melting be caused by flat subduction? Geology 28, 535–538.

Guynn, J.H., Kapp, P., Pullen, A., Gehrels, G., Heizler, M., Ding, L., 2006. Tibetan basement rocks near Amdo reveal "missing" Mesozoic tectonism along the Bangong suture, central Tibet. Geology 34, 505–508.

Guynn, J., Kapp, P., Gehrels, G.E., Ding, L., 2012. U–Pb geochronology of basement rocks in central Tibet and paleogeographic implications. Journal of Asian Earth Sciences 43, 23–50.

Harris, N.B.W., Xu, R.H., Lewis, C.L., Hawkesworth, C.J., Zhang, Y.Q., 1988. Isotope geochemistry of the 1985 Tibet Geotraverse: Lhasa to Golmud. Philosophical Transactions of the Royal Society of London. Series A 327, 263–285.

Harris, N.B.W., Inger, S., Xu, R.H., 1990. Cretaceous plutonism in central Tibet: an example of post-collision magmatism? Journal of Volcanology and Geothermal Research 44, 21–32.

He, S.D., Kapp, P., DeCelles, P.G., Gehrels, G.E., Heizler, M., 2007. Cretaceous-Tertiary geology of the Gangdese Arc in the Linzhou area, southern Tibet. Tectonophysics 433, 15–37.

Hibbard, M.J., 1991. Textural anatomy of twelve magma-mixed granitoid systems. In: Didier, J., Barbarin, B. (Eds.), Enclaves and Granite Petrology. Developments in Petrology, vol. 13. Elsevier, Amsterdam, pp. 431–444.

Holden, P., Halliday, A.N., Stephens, W.E., 1987. Neodymium and strontium isotope content of microdiorite enclaves points to mantle input to granitoid production. Nature 330, 53–56.

Holden, P., Halliday, A.N., Stephens, W.E., Henney, P.J., 1991. Chemical and isotopic evidence for major mass transfer between mafic enclaves and felsic magma. Chemical Geology 92, 135–152.

Hoskin, P.W.O., Schaltegger, U., 2003. The composition of zircon and igneous and metamorphic petrogenesis. Reviews in Mineralogy and Geochemistry 53, 27–62.

Hou, Z.Q., Gao, Y.F., Qu, X.M., Rui, Z.Y., Mo, X.X., 2004. Origin of adakitic intrusives generated during mid-Miocene east–west extension in southern Tibet. Earth and Planetary Science Letters 220, 139–155.

Hu, Z.C., Gao, S., Liu, Y.S., Hu, S.H., Chen, H.H., Yuan, H.L., 2008. Signal enhancement in laser ablation ICP-MS by addition of nitrogen in the central channel gas. Journal of Analytical Atomic Spectrometry 23, 1093–1101.

Huang, Y., Zhao, Z.D., Zhang, F.Q., Zhu, D.C., Dong, G.C., Zhou, S., Mo, X.X., 2010. Geochemistry and implication of the Gangdese batholiths from Renbu and Lhasa areas in southern Gangdese, Tibet. Acta Petrologica Sinica 26, 3131–3142 (Chinese with English abstract).

Ji, W.Q., Wu, F.Y., Chung, S.L., Li, J.X., Liu, C.Z., 2009. Zircon U–Pb geochronology and Hf isotopic constraints on petrogenesis of the Gangdese batholith, southern Tibet. Chemical Geology 262, 229–245.

Jiang, Z.Q., Wang, Q., Li, Z.X., Wyman, D.A., Tang, G.J., Jia, X.H., Yang, Y.H., 2012. Late Cretaceous (ca. 90 Ma) adakitic intrusive rocks in the Kelu area, Gangdese belt (southern Tibet): slab melting and implications for Cu–Au mineralization. Journal of Asian Earth Sciences 53, 67–81.

Kapp, P., Murphy, M.A., Yin, A., Harrison, T.M., Ding, L., Guo, J., 2003. Mesozoic and Cenozoic tectonic evolution of the Shiquanhe area of western Tibet. Tectonics 22, 1029. http://dx.doi.org/10.1029/2001TC001332.

Kapp, P., Yin, A., Harrison, T.M., Ding, L., 2005. Cretaceous-Tertiary shortening, basin development, and volcanism in central Tibet. Geological Society of America Bulletin 117, 865–878. http://dx.doi.org/10.1130/B25595.1.

Kay, R.W., Kay, S.M., 1993. Delamination and delamination magmatism. Tectonophysics 219, 177–189.

Kaygusuz, A., Aydınçakır, 2009. Mineralogy, whole-rock and Sr–Nd isotope geochemistry of mafic microgranular enclaves in Cretaceous Dagbasi granitoids, Eastern Pontides,

NE Turkey: evidence of magma mixing, mingling and chemical equilibration. Chemie der Erde-Geochemistry 69, 247–277.
Kelemen, P.B., Hart, S.R., Bernstein, S., 1998. Silica enrichment in the continental upper mantle via melt/rock reaction. Earth and Planetary Science Letters 164, 387–406.
Kent, A.J.R., Darr, C., Koleszar, A.M., Salisbury, M.J., Cooper, K.M., 2010. Preferential eruption of andesitic magmas through recharge filtering. Nature Geoscience 3, 631–636.
Keto, L.S., Jacobsen, S.B., 1987. Nd and Sr isotopic variations of Early Paleozoic oceans. Earth and Planetary Science Letters 84, 27–41.
Kocak, K., Zedef, V., Kansun, G., 2011. Magma mixing/mingling in the Eocene Horoz (Nigde) granitoids, Central southern Turkey: evidence from mafic microgranular enclaves. Mineralogy and Petrology 103, 149–167.
Le Maitre, R.W., 2002. Igneous Rocks: A Classification and Glossary of Terms, 2nd edition. Cambridge University Press 33–39.
Lee, H.Y., Chung, S.L., Lo, C.H., Ji, J., Lee, T.Y., Qian, Q., Zhang, Q., 2009. Eocene Neotethyan slab breakoff in southern Tibet inferred from the Linzizong volcanic record. Tectonophysics 477, 20–35.
Leier, A.L., DeCelles, P.G., Kapp, P., Ding, L., 2007. The Takena Formation of the Lhasa terrane, southern Tibet: the record of a Late Cretaceous retroarc foreland basin. Geological Society of America Bulletin 119, 31–48.
Lesher, C.E., 1990. Decoupling of chemical and isotopic exchange during magma mixing. Nature 344, 235–237.
Liu, Y.S., Gao, S., Yuan, H.L., Zhou, L., Liu, X.M., Wang, X.C., Hu, Z.C., Wang, L.S., 2004. U–Pb zircon ages and Nd, Sr, and Pb isotopes of lower crustal xenoliths from North China Craton: insights on evolution of lower continental crust. Chemical Geology 211, 87–109.
Liu, Q.S., Jiang, W., Jian, P., Ye, P.S., Wu, Z.H., Hu, D.G., 2006. The zircon SHRIMP U–Pb age and petrochemical and geochemical features of Mesozoic muscovite monzogranite at Ningzhong, Tibet. Acta Petrologica Sinica 22, 643–652 (in Chinese with English abstract).
Liu, Y.S., Hu, Z.C., Gao, S., Günther, D., Xu, J., Gao, C.G., Chen, H.H., 2008. In situ analysis of major and trace elements of anhydrous minerals by LA–ICP-MS without applying an internal standard. Chemical Geology 257, 34–43.
Liu, Y.S., Hu, Z.C., Zong, K.Q., Gao, C.G., Gao, S., Xu, J.A., Chen, H.H., 2010. Reappraisement and refinement of zircon U–Pb isotope and trace element analyses by LA–ICP-MS. Chinese Science Bulletin 55, 1535–1546.
Liu, D., Zhao, Z.D., Zhu, D.C., Wang, Q., Sui, Q.L., Liu, Y.S., Hu, Z.C., Mo, X.X., 2011. The petrogenesis of postcollisional potassic–ultrapotassic rocks in Xungba basin, western Lhasa terrane: constraints from zircon U–Pb geochronology and geochemistry. Acta Petrologica Sinica 27, 2045–2059 (Chinese with English abstract).
Ludwig, K., 2003. Isoplot/Ex Version 3.00: a geological toolkit for Microsoft Excel. Special Publication, 4. Berkeley Geochronology Center (70 pp.).
Ma, G.L., Yue, Y.H., 2010. Cretaceous volcanic rocks in northern Lhasa Block: constraints on the tectonic evolution of the Gangdise Arc. Acta Petrologica et Mineralogica 29, 525–538 (Chinese with English abstract).
Maniar, P.D., Piccoli, P.M., 1989. Tectonic discrimination of granitoids. Geological Society of America Bulletin 101, 635–643.
Martin, H., Smithies, R.H., Rapp, R., Moyen, J.F., Champion, D., 2005. An overview of adakite, tonalite–trondhjemite–granodiorite (TTG), and sanukitoid: relationships and some implications for crustal evolution. Lithos 79, 1–24.
Meng, F.Y., Zhao, Z.D., Zhu, D.C., Zhang, L.L., Guan, Q., Liu, M., Yu, F., Mo, X.X., 2010. Petrogenesis of Late Cretaceous adakite-like rocks in Mamba from the eastern Gangdese, Tibet. Acta Petrologica Sinica 26, 2180–2192 (Chinese with English abstract).
Miller, C., Schuster, R., Klötzli, U.S., Frank, W., Purtscheller, F., 1999. Post-collisional potassic and ultrapotassic magmatism in SW Tibet: Geochemical and Sr–Nd–Pb–O isotopic constrains for mantle source characteristics and petrogenesis. Journal of Petrology 40, 1399–1424.
Mo, X.X., Dong, G.C., Zhao, Z.D., Guo, T.Y., Wang, L.L., Chen, T., 2005. Timing of magma mixing in the Gangdise magmatic belt during the India0Asia collision: zircon SHRIMP U–Pb dating. Acta Geologica Sinica 79, 66–76.
Mo, X.X., Hou, Z.Q., Niu, Y.L., Dong, G.C., Qu, X.M., Zhao, Z.D., Yang, Z.M., 2007. Mantle contributions to crustal thickening during continental collision: evidence from Cenozoic igneous rocks in southern Tibet. Lithos 96, 225–242.
Mo, X.X., Niu, Y.L., Dong, G.C., Zhao, Z.D., Hou, Z.Q., Zhou, S., Ke, S., 2008. Contribution of syncollisional felsic magmatism to continental crust growth: a case study of the Paleogene Linzizong volcanic Succession in southern Tibet. Chemical Geology 250, 49–67.
Nowell, G.M., Kempton, P.D., Noble, S.R., Fitton, J.G., Saunders, A.D., Mahoney, J.J., Taylor, R.N., 1998. High precision Hf isotope measurements of MORB and OIB by thermal ionisation mass spectrometry: insights into the depleted mantle. Chemical Geology 149, 211–233.
Pan, G.T., Zheng, H.X., Xu, Y.Y., 1983. A preliminary study on Bangong Co–Nujiang suture. Contribution to the Geology of the Qinghai Xizang 12, 229–242.
Pan, G.T., Ding, J., Yao, D.S., Wang, L.Q., 2004. Guidebook of 1:1500000 geologic map of the Qinghai–Xizanf (Tibet) plateau and adjacent areas. Chengdu, China, Chengdu Cartographic Publishing House, 1–48 (in Chinese).
Pearce, J.A., Deng, W.M., 1988. The ophiolites of the Tibetan geotraverses, Lhasa to Golmud (1985) and Lhasa to Kathmandu (1986). Philosophical Transactions of the Royal Society of London. Series A, Mathematical and Physical Sciences 327, 215–238.
Pearce, J.A., Norry, M.J., 1979. Petrogenetic implications of Ti, Zr, Y and Nb variations in volcanic rocks. Contributions to Mineralogy and Petrology 69, 33–47.
Perugini, D., Poli, G., Christofides, G., Eleftheriadis, G., 2003. Magma mixing in the Sithonia Plutonic Complex, Greece: evidence from mafic microgranular enclaves. Mineralogy and Petrology 78, 173–200.
Pin, C., Binon, M., Belin, J.M., Barbarin, B., Clemens, J.D., 1990. Origin of microgranular enclaves in granitoids: equivocal Sr–Nd evidence from Hercynian rocks in the Central France. Journal of Geophysical Research 95, 17821–17828.
Poli, G.E., Tommasini, S., 1991. Model for the origin and significance of microgranular enclaves in calc-alkaline granitoids. Journal of Petrology 32, 657–666.
Qu, X.M., Xin, H.B., Xu, W.Y., Yang, Z.S., Li, Z.Q., 2006. Discovery and significance of copper-bearing bimodal rock series in Coqin area of Tibet. Acta Petrologica Sinica 22, 707–716 (Chinese with English abstract).
Quidelleur, X., Grove, M., Lovera, O.M., Harrison, T.M., Yin, A., Ryerson, F., 1997. Thermal evolution and slip history of the Renbu Zedong Thrust, southeastern Tibet. Journal of Geophysical Research 102, 2659–2679.
Rapp, R.P., Shimizu, N., Norman, M.D., Applegate, G.S., 1999. Reaction between slab-derived melts and peridotite in the mantle wedge: experimental constraints at 3.8 GPa. Chemical Geology 160, 335–356.
Rudnick, R.L., Fountain, D.M., 1995. Nature and composition of the continental crust: a lower crustal perspective. Reviews of Geophysics 33, 267–309.
Rudnick, R.L., Shan, G., Ling, W.L., Liu, Y.S., McDonough, W.F., 2004. Petrology and geochemistry of spinel peridotite xenoliths from Hannuoba and Qixia, North China craton. Lithos 77, 609–637.
Schonenberger, J., Marks, M., Wagner, T., Markl, G., 2006. Fluid–rock interaction in autoliths of agpaitic nepheline syenites in the Ilimaussaq intrusion, South Greenland. Lithos 91, 331–351.
Sengör, A.M.C., 1987. Tectonics of the Tethysides: orogenic collage development in a collisional setting. Annual Review of Earth and Planetary Sciences 15, 213–244.
Shellnutt, J., Jahn, B.M., Dostal, J., 2010. Elemental and Sr–Nd isotope geochemistry of microgranular enclaves from peralkaline A-type granitic plutons of the Emeishan large igneous province, SW China. Lithos 119, 34–46.
Sheppard, S., Griffin, T., Tyler, I., Page, R., 2001. High-and low-K granites and adakites at a Palaeoproterozoic plate boundary in northwestern Australia. Journal of the Geological Society 158, 547–560.
Söderlund, U., Patchett, P.J., Vervoort, J.D., Isachsen, C.E., 2004. The ^{176}Lu decay constant determined by Lu–Hf and U–Pb isotope systematics of Precambrian mafic intrusions. Earth and Planetary Science Letters 219, 311–324.
Sun, S.S., McDonough, W.F., 1989. Chemical and isotope systematics of oceanic basalts: implications for mantle composition and processes. In: Saunders, A.D. (Ed.), Magmatism in Ocean Basins. Geological Society Publication, 42, pp. 313–345.
Vernon, R.H., 1984. Microgranitoid enclaves in granites-globules of hybrid magma quenched in a plutonic environment. Nature 309, 438–439.
Vernon, R.H., 1990. Crystallization and hybridism in micro-granitoid enclave magmas: microstructural evidence. Journal of Geophysical Research 95, 17849–17859.
Volkmer, J.E., Kapp, P., Guynn, J.H., Lai, Q., 2007. Cretaceous-Tertiary structural evolution of the north central Lhasa terrane, Tibet. Tectonics 26. http://dx.doi.org/10.1029/2005TC001832.
Waight, T.E., Maas, R., Nicholls, I.A., 2000. Fingerprinting feldspar phenocrysts using crystal isotopic composition stratigraphy: implications for crystal transfer and magma mingling in S-type granites. Contributions to Mineralogy and Petrology 139, 227–239.
Wang, Q., McDermott, F., Xu, J.F., Bellon, H., Zhu, Y.T., 2005. Cenozoic K-rich adakitic volcanic rocks in the Hohxil area, northern Tibet: lower-crustal melting in an intracontinental setting. Geology 33, 465–468.
Wang, Q., Wyman, D., Zhao, Z., Xu, J., Bai, Z., Xiong, X., Dai, T., Li, C., Chu, Z., 2007. Petrogenesis of Carboniferous adakites and Nb-enriched arc basalts in the Alataw area, northern Tianshan Range (western China): implications for Phanerozoic crustal growth in the Central Asia orogenic belt. Chemical Geology 236, 42–64.
Wang, Q., Li, X.H., Jia, X.H., Wyman, D., Tang, G.J., Li, Z.X., Ma, L., Yang, Y.H., Jiang, Z.Q., Gou, G.N., 2012. Late Early Cretaceous adakitic granitoids and associated magnesian and potassium-rich mafic enclaves and dikes in the Tunchang–Fengmu area, Hainan Province (South China): partial melting of lower crust and mantle, and magma hybridization. Chemical Geology 328, 222–243.
Weinberg, R.F., Sial, A.N., Pessoa, R.R., 2001. Magma flow within the travers pluton, northeastern Brazil: compositional and thermal convection. Geological Society of America Bulletin 113, 508–520.
Wen, D.R., Chung, S.L., Song, B., Iizuka, Y., Yang, H.J., Ji, J.Q., Liu, D.Y., Gallet, S., 2008a. Late Cretaceous Gangdese intrusions of adakitic geochemical characteristics, SE Tibet: petrogenesis and tectonic implications. Lithos 105, 1–11.
Wen, D.R., Liu, D., Chung, S.L., Chu, M.F., Ji, J., Zhang, Q., Song, B., Lee, T.Y., Yeh, M.W., Lo, C.H., 2008b. Zircon SHRIMP U–Pb ages of the Gangdese Batholith and implications for Neotethyan subduction in southern Tibet. Chemical Geology 252, 191–201.
Wiebe, R.A., Smith, D., Stum, M., King, E.M., Seckler, M.S., 1997. Enclaves in the Cadillac mountain granite (Coastal Maine): samples of hybrid magma from the base of the chamber. Journal of Petrology 38, 393–423.
Wiedenbeck, M., Alle, P., Corfu, F., Griffin, W., Meier, M., Oberli, F., Quadt, A., Roddick, J., Spiegel, W., 1995. Three natural zircon standards for U–Th–Pb, Lu–Hf, trace element and REE analyses. Geostandards Newsletter 19, 1–23.
Wilson, M., 1989. Igneous Petrogenesis. Unwim Hyman, London 1–366.
Wyllie, P.J., Cox, K.G., Biggar, G.M., 1962. The habit of apatite in synthetic systems and igneous rocks. Journal of Petrology 3, 238–243.
Xu, R.H., Scharer, U., Allegre, C.J., 1985. Magmatism and metamorphism in the Lhasa Block (Tibet)—a geochronological study. Journal of Geology 93, 41–57.
Xu, W.L., Gao, S., Wang, Q.H., Wang, D.Y., Liu, Y.S., 2006. Mesozoic crustal thickening of the eastern North China craton: evidence from eclogite xenoliths and petrologic implications. Geology 34, 721–724.
Xu, H.J., Ma, C.Q., Zhang, J.F., 2012. Generation of Early Cretaceous high-Mg adakitic host and enclaves by magma mixing, Dabie orogen, Eastern China. Lithos 142–143, 182–200.
Yang, D.M., He, Z.H., Wang, T.W., 2005. 1:250,000 mapping investigation of Mamba Area, P. R. China. Unpublished (in Chinese).
Yang, J.H., Wu, F.Y., Chung, S.L., Wilde, S.A., Chu, M.F., 2006. A hybrid origin for the Qianshan A-type granite, northeast China: geochemical and Sr–Nd–Hf isotopic evidence. Lithos 89, 89–106.

Yang, J.H., Wu, F.Y., Wilde, S.A., Xie, L.W., Yang, Y.H., Liu, X.M., 2007. Tracing magma mixing in granite genesis: in situ U–Pb dating and Hf-isotope analysis of zircons. Contributions to Mineralogy and Petrology 153, 177–190.

Ye, L., 2013. Chronology and Geochemistry of Magmatic Rocks in Namling–Yangbajing at Lhasa Terrane, Tibet. China University of Geosciences, Beijing 1–85 (Bachelor thesis).

Yin, A., Harrison, T.M., 2000. Geologic evolution of the Himalayan–Tibetan orogen. Annual Review of Earth and Planetary Sciences 28, 211–280.

Yin, J.X., Xu, J.T., Liu, C.J., Li, H., 1988. The Tibetan plateau: regional stratigraphic context and previous work. Philosophical Transactions of the Royal Society of London. Series A, Mathematical and Physical Sciences 5–52.

Yu, H.X., Chen, J.L., Xu, J.F., Wang, B.D., Wu, J.B., Liang, Y.H., 2011. Geochemistry and origin of Late Cretaceous (~90 Ma) ore-bearing porphyry of Balazha in mid-northern Lhasa terrane, Tibet. Acta Petrologica Sinica 27, 2011–2022 (Chinese with English abstract).

Yuan, H.L., Gao, S., Dai, M.N., Zong, C.L., Gunther, D., Fontaine, G.H., Liu, X.M., Diwu, C., 2008. Simultaneous determinations of U–Pb age, Hf isotopes and trace element compositions of zircon by excimer laser-ablation quadrupole and multiple-collector ICP-MS. Chemical Geology 247, 100–118.

Zhang, Z.M., Zhao, G.C., Santosh, M., Wang, J.L., Dong, X., Shen, K., 2010a. Late Cretaceous charnockite with adakitic affinities from the Gangdese batholith, southeastern Tibet: evidence for Neo-Tethyan mid-ocean ridge subduction? Gondwana Research 17, 615–631.

Zhang, Z.M., Dong, X., Geng, G.S., Wang, W., Yu, F., Liu, F., 2010b. Precambrian metamorphism of the northern Lhasa Terrane, south Tibet and its tectonic implications. Acta Geologica Sinica 84, 449–456 (in Chinese with English abstract).

Zhang, Z.M., Shen, K., Santosh, M., Dong, X., 2011. High density carbonic fluids in a slab window: evidence from the Gangdese charnockite, Lhasa terrane, southern Tibet. Journal of Asian Earth Sciences 42, 515–524.

Zhang, Z.M., Dong, X., Liu, F., Lin, Y.H., Yan, R., He, Z.Y., Santosh, M., 2012. The making of Gondwana: discovery of 650 Ma HP granulites from the North Lhasa, Tibet. Precambrian Research 212–213, 107–116.

Zhang, Z.M., Dong, X., Santosh, M., Zhao, G.C., 2013. Metamorphism and tectonic evolution of the Lhasa terrane, Central Tibet. Gondwana Research. http://dx.doi.org/10.1016/j.gr.2012.08.024.

Zhao, Z., Mo, X., Dilek, Y., Niu, Y., DePaolo, D.J., Robinson, P., Zhu, D., Sun, C., Dong, G., Zhou, S., 2009. Geochemical and Sr–Nd–Pb–O isotopic compositions of the post-collisional ultrapotassic magmatism in SW Tibet: petrogenesis and implications for India intra-continental subduction beneath southern Tibet. Lithos 113, 190–212.

Zhao, Z.D., Zhu, D.C., Dong, G.C., Mo, X.X., DePaolo, D., Jia, L.L., Hu, Z.C., Yuan, H.L., 2011. The ~54 Ma gabbro-granite intrusive in southern Dangxung area, Tibet petrogenesis and implications. Acta Petrologica Sinica 27, 3513–3524 (Chinese with English abstract).

Zhu, D.C., Mo, X.X., Pan, G.T., Zhao, Z.D., Dong, G.C., Shi, Y.R., Liao, Z.L., Wang, L.Q., Zhou, C.Y., 2008a. Petrogenesis of the earliest Early Cretaceous mafic rocks from the Cona area of the eastern Tethyan Himalaya in south Tibet: interaction between the incubating Kerguelen plume and the eastern Greater India lithosphere? Lithos 100, 147–173.

Zhu, D.C., Mo, X.X., Zhao, Z.D., Xu, J.F., Zhou, C.Y., Sun, C.G., Wang, L.Q., Chen, H.H., Dong, G.C., Zhou, S., 2008b. Zircon U–Pb geochronology of Zenong Group volcanic rocks in Coqen area of the Gangdese, Tibet and tectonic significance. Acta Petrologica Sinica 24, 401–412 (in Chinese with English abstract).

Zhu, D.C., Mo, X.X., Niu, Y.L., Zhao, Z.D., Wang, L.Q., Liu, Y.S., Wu, F.Y., 2009a. Geochemical investigation of Early Cretaceous igneous rocks along an east–west traverse throughout the central Lhasa Terrane, Tibet. Chemical Geology 268, 298–312.

Zhu, D.C., Mo, X.X., Wang, L.Q., Zhao, Z.D., Niu, Y.L., Zhou, C.Y., Yang, Y.H., 2009b. Petrogenesis of highly fractionated I-type granites in the Zayu area of eastern Gangdese, Tibet: constraints from zircon U–Pb geochronology, geochemistry and Sr–Nd–Hf isotopes. Science in China Series D: Earth Sciences 52, 1223–1239.

Zhu, D.C., Zhao, Z.D., Pan, G.T., Lee, H.Y., Kang, Z.Q., Liao, Z.L., Wang, L.Q., Li, G.M., Dong, G.C., Liu, B., 2009c. Early cretaceous subduction-related adakite-like rocks of the Gangdese Belt, southern Tibet: products of slab melting and subsequent melt–peridotite interaction? Journal of Asian Earth Sciences 34, 298–309.

Zhu, D.C., Zhao, Z.D., Niu, Y., Mo, X.X., Chung, S.L., Hou, Z.Q., 2011a. The Lhasa Terrane: record of a microcontinent and its histories of drift and growth. Earth and Planetary Science Letters 301, 241–255.

Zhu, D.C., Zhao, Z.D., Niu, Y.L., Dilek, Y., Mo, X.X., 2011b. Lhasa terrane in southern Tibet came from Australia. Geology 39, 727–730.

Zhu, D.C., Zhao, Z.D., Niu, Y.L., Dilek, Y., Hou, Z.Q., Mo, X.X., 2013. The origin and pre-Cenozoic evolution of the Tibetan Plateau. Gondwana Research 23, 1429–1454.